

# Modeling UX Ursae Majoris<sup>1</sup>: An abundance of challenges.

Albert P. Linnell<sup>2</sup>, Patrick Godon<sup>3</sup>, Ivan Hubeny<sup>4</sup>, Edward M. Sion<sup>5</sup>, Paula Szkody<sup>6</sup>

<sup>2</sup>*Department of Astronomy, University of Washington, Box 351580, Seattle, WA  
98195-1580*

<sup>3</sup>*Department of Astronomy and Astrophysics, Villanova University, Villanova, PA 19085  
visiting at the Space Telescope Institute, Baltimore, MD.*

<sup>4</sup>*Steward Observatory and Department of Astronomy, University of Arizona, Tucson, AZ  
85721*

<sup>5</sup>*Department of Astronomy and Astrophysics, Villanova University, Villanova, PA 19085*

<sup>6</sup>*Department of Astronomy, University of Washington, Box 351580, Seattle, WA  
98195-1580*

<sup>2</sup>linnell@astro.washington.edu

<sup>3</sup>godon@stsci.edu

<sup>4</sup>hubeny@as.arizona.edu

<sup>5</sup>edward.sion@villanova.edu

<sup>6</sup>szkody@astro.washington.edu

## ABSTRACT

We present a system model for optical and far UV spectra of the nova-like variable UX UMA involving a white dwarf, secondary star, gas stream, hot spot and accretion disk using our code BINSYN and based on an initially adopted system distance. Calculated SED intensity data successfully fit successive tomographically-extracted annuli longward of the Balmer limit but require a postulated ‘iron curtain’ shortward of the Balmer limit that is applied to the annulus section closest to the secondary star, while postulated recombination emission fills in the model SED shortward of the Balmer limit and is applied to the annulus section more remote from the secondary star. The same model fits *UBV* 1954 light curves by Walker and Herbig. Fits to *HST FOS* spectra are approximate but require assumed time-variable changes in the SED. Comparable effects, possibly involving variable absorption, afflict *FUSE* spectra. Fits to

---

<sup>1</sup>Based on observations made with the NASA/ESA Hubble Space Telescope, obtained at the Space Telescope Science Institute, which is operated by the Association of Universities for Research in Astronomy, Inc. under NASA contract NAS5-26555, and the NASA-CNES-CSA *Far Ultraviolet Explorer*, which is operated for NASA by the Johns Hopkins University under NASA contract NAS5-32985.

*IUE* spectra by the model show time-dependent residuals that indicate changes in the accretion disk temperature profile, possibly indicative of a slightly variable  $\dot{M}$  from the secondary star. Using model-based component light contributions and the improvement on the Bailey relation by Knigge we determine the system distance and mass transfer rate.

*Subject headings:* accretion, accretion disks — novae, cataclysmic variables — stars: individual(UX UMa) — ultraviolet: stars — white dwarfs

## 1. Introduction

Cataclysmic variables (CVs) are semi-detached binary stars in which a late-type typically main sequence star loses mass onto a white dwarf (WD) via Roche lobe overflow and accretion proceeds through a viscous disk. In the nova-like (NL) subclass, of which UX UMa is the prototype, the mass transfer rate from the secondary star is large enough that dwarf nova outbursts do not occur. (See Warner (1995) for a history of UX UMa studies and a thorough review of CV types and properties.) Important early studies of UX UMa by Walker & Herbig (1954); Johnson, Perkins, & Hiltner (1954) and Krzemiński & Walker (1963) established the system photometric properties, while Nather & Robinson (1974) discovered coherent oscillations. *IUE* spectra identified UX UMa as a UV emission line variable (Holm, Panek, & Schiffer 1982; King et al. 1983). X-ray observations (Becker 1981; Wood, Naylor, & Marsh 1995) detected a soft source, further refined (Pratt et al. 2004) to a noneclipsed soft component and a deeply eclipsed hard component. An accretion disk wind was discovered by Mason et al. (1995) and modeled by Knigge & Drew (1997).

Knigge et al. (1998a) had mixed success in modeling the spectral energy distribution (SED) of UX UMa with a combination of stellar atmosphere synthetic spectra. A similar approach by Froning et al. (2003) (hereafter FR2003) in a fit to the *FUSE* spectrum produced an estimated  $\dot{M} = 1.6 \times 10^{-9} M_{\odot} \text{ yr}^{-1}$ . However, a mass transfer rate of  $\dot{M} = 1.6 \times 10^{-9} M_{\odot} \text{ yr}^{-1}$  is small enough that the system would be unstable against outburst, contrary to observation. Neither of these two studies included a SED contribution from the WD; on the other hand, tomographic reconstruction of the UX UMa disk (Rutten et al. 1992) is consistent with a standard model accretion disk with  $\dot{M} = 5 \times 10^{-9} M_{\odot} \text{ yr}^{-1}$ . A comparable study by Baptista et al. (1995) hereafter BA1995, with a different estimated distance to the system, finds  $\dot{M} = 1 \times 10^{-8} M_{\odot} \text{ yr}^{-1}$ . Frank et al. (1981) modeled IR and optical light curves and determined system parameters. Smak (1994a) modeled optical region light curves and derived bright spot parameters. Mason, Drew, & Knigge (1997) argue that a more complicated structure than a bright spot on an otherwise unmodified accretion

disk rim is necessary. BA1995 derived a WD  $T_{\text{eff}}$  of 52,000K to 70,000K, but FR2003 points out that a  $T_{\text{eff}}$  that large is inconsistent with FUV spectra. Neither of the tomographic reconstruction studies has been the basis of an effort to model the spectra. These continuing inconsistencies are the motivation to attempt to derive a single model that represents a substantial part of the disparate observational data.

## 2. Observational Data: Spectroscopic and Photometric Observations

Table 1 lists the spectroscopic observations used in this study. We obtained the *IUE* spectra from the *IUE* archive and processed them with the standard IUEDAC package. The *HST/FOS* observations are from Knigge et al. (1998a), further analyzed in Baptista et al. (1998), hereafter BA1998, and described in that publication: the G160L data sets each include 691 spectra and the PRISM data sets each include 870 spectra; these time-resolved spectra have a resolution of 5.3 s. We obtained the time-integrated spectrum of each of the G160L data sets from the MAST archive for our analysis and designate this data set DS1. We used spectroscopic data from the Rutten et al. (1994) paper, consisting of optical spectra obtained in June 1992; we designate this data set DS2. For that data set we used the Dexter facility of the Astrophysics Data Service (ADS) to digitize the spectrally-resolved disk spectra for regions A-F in their Figures 5a-f.

In agreement with Rutten et al. (1992), we adopt an interstellar reddening of  $E(B - V) = 0.0$ . Bruch & Engel (1994) list  $E(B - V) = 0.02$ . This small value is uncertain because of the variability of the system light curve discussed below and we prefer to leave the reddening at 0.0 for our analysis. Unless stated otherwise, changing to  $E(B - V) = 0.02$  has a negligible effect on our results. The *FUSE* spectra, from the MAST archive (and used by FR2003), were processed with CalFUSE v3.1. The dataset includes multiple exposures; we have selected two for this study. The *HST/FOS* spectral lines were identified and studied by Knigge et al. (1998a) and BA1998 while the *FUSE* spectral lines were identified and studied by FR2003; we do not repeat those identifications.

## 3. Initial System Parameters

Rutten et al. (1992) list several determinations of the distance to UX UMA and adopt a compromise value of 250pc. Additional determinations are Smak (1994a) ( $328 \pm 12$ pc), Frank et al. (1981) ( $340 \pm 110$ pc), and BA1995 ( $345 \pm 34$ pc). FR2003 challenge the BA1995 system parameters, and our analysis agrees with some of the FR2003 points. (We have

concerns about the BA1995 determination; see §6.) We choose to adopt the distance of 250pc for our working model, initially as an illustrative test and subject to subsequent consistency verification. The distance uncertainty remains a major obstacle and there is a degeneracy between the system distance and the adopted  $\dot{M}$ .

Rutten et al. (1994) determined an approximate spectral type of M0 for the secondary star in UX UMa and a corresponding main sequence mass of  $\sim 0.5M_{\odot}$ . This determination, together with the orbital period, is consistent with the Smak (1994a) system parameters of  $M_{\text{wd}} = 0.70 \pm 0.2M_{\odot}$ ,  $M_s = 0.49M_{\odot}$ , and  $q = 0.70$ . The period-secondary mass relation of Warner (1995, eq. 2.100) gives a secondary mass of  $M_s = 0.48M_{\odot}$ , while the Knigge (2006) period-secondary mass relation finds  $M_s = 0.44M_{\odot}$ . A radial velocity study by Shafter (1984) finds that  $M_s \lesssim 0.5M_{\odot}$  and the mass ratio of the system is greater than  $\sim 0.8$ . Frank et al. (1981) find  $0.2 < M_s/M_{\odot} < 0.5$  and  $0.1 < M_{\text{wd}}/M_{\odot} < 0.5$ . They also find  $\dot{M} = 8 \times 10^{-9} M_{\odot} \text{ yr}^{-1}$  (see below). It is worth mentioning that, at an orbital period of  $4.7^h$ , UX UMa lies in a region of parameter space where nuclear evolution of secondaries becomes significant, adding a measure of uncertainty to standard relationships.

The BA1995  $M_{\text{wd}} = 0.47M_{\odot}$  depends on the radial velocity value  $K_{\text{wd}} = 160 \text{ km s}^{-1}$  (Shafter 1984) determined from the emission wings of  $\text{H}\alpha$ . Schlegel, Honeycutt, & Kaitchuck (1983) found a range of  $K_{\text{wd}}$  values for different spectral features. FR2003 used a cross-correlation procedure to determine a  $K_{\text{wd}}$  of  $70 \text{ km s}^{-1}$ , while absorption reversals in emission lines determined  $K_{\text{wd}}$  values from  $140 \text{ km s}^{-1}$  for S IV and S III to  $200 \text{ km s}^{-1}$  for C III. Thus there is some uncertainty in the  $M_{\text{wd}}$  determination; a more secure value of  $M_{\text{wd}}$  depends on an improved radial velocity curve attributable to the WD. Note that the value  $q = 1$  is at the limit of stability against dynamical mass transfer which occurs for  $q > 1$ . We provisionally adopt the BA1995 model,  $M_{\text{wd}} = M_s = 0.47M_{\odot}$ . This model closely agrees with the model adopted by Rutten et al. (1992, Table 4),  $M_{\text{wd}} = M_s = 0.45M_{\odot}$ .

From Panei, Althaus, & Benvenuto (2000), the zero temperature radius of a  $0.47M_{\odot}$  WD is  $R_{\text{wd},0} = 0.01375R_{\odot} = 9.57 \times 10^8 \text{ cm}$  and, from their Fig.4a, we find that the radius of a 20,000K,  $0.47M_{\odot}$  WD, used later in our discussion, would be  $1.15 \times 10^9 \text{ cm}$ . BA1995 argue that, if 1/2 of the WD is visible, it has a  $T_{\text{eff}} = 70,000 \text{ K}$ . This temperature is off the Figure 4a plot of Panei, Althaus, & Benvenuto (2000), but we estimate a radius of  $3.5 \times 10^9 \text{ cm}$ . A 70,000K WD with this radius (and visible to the observer) would completely dominate the system flux and would lead to a seriously discrepant synthetic spectrum (see below). (Also see the discussion by FR2003.)

Table 2 lists the system parameters used in this paper. Except for  $i$  the parameters are adopted as discussed herein and so have no errors attached. The Roche potential for the WD produces a radius appropriate to a  $0.47M_{\odot}$ , 20,000K WD. The secondary star Roche

potential causes it to fill its Roche lobe. Rutten et al. (1992) find  $i = 71^\circ$  for their  $q = 1.0$  model. They investigate the sensitivity of this result to variation of  $q$  and  $i$ , and find their result is not very sensitive provided the eclipse width remains unchanged. In our light curve simulations (§4.1) we found a slight improvement in the fit to eclipse depth with  $i = 70.2^\circ$ , but a detectably poorer fit to eclipse width with  $i = 70.0^\circ$ . We adopt  $i = 70.2^\circ$ .

Using a maximum-entropy eclipse mapping algorithm (the MEM method), Rutten et al. (1992) determine a temperature profile for the UX UMa accretion disk (their Figure 4b). The procedure uses four optical-wavelength eclipse light curves that constitute the observational data. A two-dimensional array of surface elements (pixels) covers the model accretion disk which is projected on the sky at inclination  $i$ . A default intensity is assigned to each pixel at each of the observed wavelengths and an assumed distance together with calibrated absolute magnitudes for the observational data produces intensities in physical units. The algorithm then iterates to vary the individual intensities until the entire calculated array of pixel intensities has maximum entropy, thereby fitting the observed light curves with calculated light curves. A black body fit to individual pixel intensities at the four observed wavelengths determines  $T_{\text{eff}}$ , pixel by pixel. The temperature profile then is a plot of the pixel  $T_{\text{eff}}$  values as function of the pixel distance from the center of the WD.

We used the ADS Dexter facility to digitize the points in their plot. We also used the Dexter facility to digitize the BA1998 ‘back’ points (discussed in §4.) from their Figure 7 for November 1994. Figure 1 compares the temperature profile in our model with the points from Rutten et al. (crosses) and Baptista et al. (triangles). Note that the plotted points do not represent directly observed quantities; rather, they are derived quantities from the maximum entropy maps. Based on the Figure 1 plot, our model adopts a standard model (Frank, King, & Raine 1992)  $\dot{M} = 5.0 \times 10^{-9} M_\odot \text{yr}^{-1}$  temperature profile as an initial approximation. By eye estimate, the temperature profile for our model is a fairly good fit to the plotted data points. The data points depart from a standard model near the L1 point where the bright spot and tidal heating exert an effect (discussed below).

There are no data points at extremely small radii; we find ambiguous evidence for obscuration of the WD and/or for a hot boundary layer, raising doubts about the justification of modeling the theoretical temperature downturn at very small radii. The theoretical downturn assumes a slowly-rotating central star (Frank, King, & Raine 1992); with faster rotation the downturn becomes smaller and we have no information on the rotation rate of the WD. Our Figure 1 profile shows only the start of a temperature drop near the WD and so fails to fit the theoretical  $\dot{M}$  profiles at small radii. Our model calculates only one annulus with radius less than the radius of the temperature maximum at  $R = 1.36R_{\text{wd}}$ .

Our program uses the Warner (1995, Equation 2.61) relation for the tidal cutoff radius

and for  $q = 1.0$  this leads to  $R_{\text{cutoff}} = 0.6R_{\text{L1}}$ . Rutten et al. (1992) and BA1998 both tabulate data points to  $R = 0.7R_{\text{L1}}$ . This difference explains the failure of our model to extend to the tabular terminus of the Rutten et al. data in Figure 1. We subsequently (§4.1) model light curves with the aid of a bright spot on the accretion disk rim. Rutten et al. (1992, Table 7) determine  $R_{\text{spot}}/R_{\text{L1}} = 0.57 \pm 0.05$ , in agreement with the rim location in our model. If our model allowed the accretion disk to extend to  $R_{\text{cutoff}} = 0.7R_{\text{L1}}$  the  $T_{\text{eff}}$  of the outermost part of the accretion disk would be below the temperature limit for stability (Osaki 1996). We do not believe the tidal cutoff sets a sharp boundary beyond which no emitting gas can be found but for formal internal consistency we adopt  $R_{\text{cutoff}} = 0.6R_{\text{L1}}$ .

### 3.1. Calculation of synthetic spectra

Our model uses the BINSYN suite (Linnell & Hubeny (1996); Linnell et al. (2008) and references therein). This model includes contributions from the accretion disk, the WD, the secondary star, and the accretion disk rim. Smak (2002) shows that the structure of the outer parts of accretion disks is an important consideration. Smak shows that allowance for tidal heating produces a rim  $T_{\text{eff}}$  comparable to that of the outermost annulus. On a finer scale, which Smak does not discuss in detail, the part of the rim close to the orbital plane has a higher  $T_{\text{eff}}$  than at a higher  $z$  value. We set the rim  $T_{\text{eff}}$  equal to that of the outermost annulus and make the rim isothermal. The program requires a set of individually-calculated accretion disk annulus spectra which are based on annulus models calculated with program TLUSTY (Hubeny 1988, 1990; Hubeny & Lanz 1995; Hubeny & Hubeny 1998). The annulus models do not include irradiation by the central star although this is a TLUSTY option; we will find there is some uncertainty concerning the WD  $T_{\text{eff}}$ . We emphasize that the TLUSTY option for accretion disk annuli (without irradiation) produces a standard model radial temperature profile and includes explicit treatment of the mass transfer rate and the WD mass and radius. It would be impractical to recalculate TLUSTY annulus model arrays for different WD radii depending on the radii appropriate to different assumed  $T_{\text{eff}}$  values. We calculate a single array appropriate to a zero temperature WD and handle the effect of a non-zero temperature WD in the BINSYN model. Table 3 lists the annuli used in our model and gives some of the individual annulus properties. The first column lists the radius of the annulus; the second column lists the  $T_{\text{eff}}$ ; the third column lists the column mass to the central plane in  $\text{gm}/\text{cm}^2$ ; the fourth column lists the temperature at the central plane; the fifth column lists  $\log g$  (cgs) at a Rosseland optical depth of approximately 0.6; the sixth column lists the vertical distance above the central plane of the optical depth 0.6 point, in cm; the final column lists the Rosseland optical depth of the central plane. The annulus model calculations through  $r/r_{\text{wd},0} = 12.0$  converged. The remaining models are grey model

solutions and are subject to some scatter in the calculated  $z_H$ . The TLUSTY models have standard model (Frank, King, & Raine 1992)  $T_{\text{eff}}$  values.

Program SYNSPEC (Hubeny, Lanz, & Jeffery 1994) uses the TLUSTY output to calculate individual annulus synthetic spectra. The spectra were calculated with a spectral resolution of  $1\text{\AA}$ . An important point is that SYNSPEC produces both of two different output formats. In one, the output is in Eddington flux units ( $\text{erg cm}^{-2} \text{s}^{-1} \text{\AA}^{-1}$ ). In the other the output is in intensities ( $\text{erg cm}^{-2} \text{s}^{-1} \text{hz}^{-1} \text{sr}^{-1}$ ) for a specified array of directions relative to the outward normal. In our calculations we specified ten directions equally spaced in  $\cos(\gamma)$ , where  $\gamma$  is the angle between the chosen direction and the outward normal to the local photosphere. We will specifically require the intensity-based data for some of the subsequent discussion.

BINSYN sets up a separate array of annuli to represent the accretion disk; in this study we used 45 division circles to produce 44 annuli, with inner radius at the WD boundary and outer radius at the tidal cutoff boundary. This choice provides adequate radial resolution for accurate calculation of both synthetic spectra and light curves. One half of the WD is visible in this model. BINSYN uses the Frank, King, & Raine (1992, eq. 5.45) equation set to calculate a standard model accretion disk, including the rim height. Table 4 lists the array properties. In calculating flux from annulus segments we use the  $T_{\text{eff}}$  of the annulus inner edge. The tabulation of accretion disk annuli from TLUSTY, Table 3, begins at the accretion disk temperature maximum since following the theoretical temperature drop to smaller radii would lead to double-value ambiguity (either side of the maximum) in the BINSYN interpolation. The algorithm for assigning radii in BINSYN places at least one division circle interior to the temperature maximum. The two initial entries with the same  $T_{\text{eff}}$  represent the inner and outer radii of the first annulus; thereafter the table lists the outer radius.

The  $T_{\text{eff}}$  values in Table 4 are appropriate for a 20,000K WD, with its radius determined as in §3. The change in WD radius from a zero temperature WD produces a clearly detectable change in the tabular values of the BINSYN annuli  $T_{\text{eff}}$  values. Compare the  $T_{\text{eff}}$  values at  $r/r_{\text{wd}} = 1.36$  in Table 3 and Table 4; the difference is due to the different values of  $r_{\text{wd}}$ . BINSYN determines flux values for segments on a given annulus by using the Table 4  $T_{\text{eff}}$  value to interpolate, temperature-wise, within Table 3, making use of the flux values corresponding to the Table 3 entries. Note that Table 3 is based on  $r_{\text{wd},0} = 9.57 \times 10^8 \text{ cm}$  while Table 4 is based on  $r_{\text{wd}}(T = 20,000\text{K}) = 1.15 \times 10^9 \text{ cm}$ .

By option, the Table 4 profile may be replaced by a different non-standard model profile. This option has been used in a number of instances (e.g., Linnell et al. (2008)).

#### 4. Comparison of model with DS1 and DS2

Our comparisons will use eclipse maps associated with the DS1 and DS2 data and these maps will require default intensities for the map pixels. Calculation of default intensities requires a source distance to determine the subtended solid angle. DS1 adopted a distance of 345pc; DS2, 250pc. Our working model adopts 250pc (§3.), so to produce a common standard of comparison we divide the first data set intensities by  $(345/250)^2 = 1.9$ . Separate tests show that our results remain essentially unchanged if we adopt a distance of 345pc, normalize observed intensities to that distance, and adopt  $\dot{M} = 1.0 \times 10^{-8} M_{\odot} \text{ yr}^{-1}$ .

Production of a MEM eclipse map, which determines intensities pixel by pixel, permits segregation of pixels into isolated regions on the accretion disk. Thus, DS1 divides the accretion disk into concentric rings, each ring further subdivided into a 'back', a 'front', and a 'stream'. Figure 2a illustrates the DS1 divisions. From §2, the observational data include both the PRISM and G160L as separate spectral sources. Consequently, it was necessary to introduce identifiers for the source of the data used as well as the position of the ring subdivision. Thus, in DS1, identifier 'prism.center' refers to the radial range  $0.000r_{L1}$ - $0.075r_{L1}$ , while the identifier 'prism.back.20' refers to the azimuthal range  $90^{\circ}$  to  $270^{\circ}$  on the annulus extending from  $0.175r_{L1}$  to  $0.225r_{L1}$ . Table 5 lists the subdivisions of the accretion disk and may be compared with Figure 2a. DS2 follows a similar but coarser scheme of geometric resolution; its subdivisions also are listed in Table 5.

The PRISM spectra were divided into 127 passbands and a separate MEM map was constructed for each passband. For each ring subdivision, concatenation of the 127 passband intensities constituted an extremely low resolution spectrum. It is that 'spectrum', for a given ring subdivision, that we fit with our model synthetic spectrum. Since the data being fit consist of intensities, it is necessary to use the corresponding intensity output from SYNSPEC as discussed in §3.1.

The G160L spectra were divided into 59 passbands and processed as with the PRISM data. DS2 used low-resolution optical wavelength spectra and followed a similar basic procedure. Note that DS2 are corrected for extinction in the Earth's atmosphere while DS1 requires no such correction.

Figure 2b illustrates the BINSYN model and the 44 annuli. Software keys isolate annuli subdivisions ('front', 'back', 'stream') for comparison with DS1. Given the Table 5 radial ranges, in each comparison we select an annulus from Table 4 that is centered on the DS1 or DS2 annulus in question.

The §3 system parameters and the  $\dot{M}$  from Figure 1 set the model scale and the radiation properties of the individual photospheric segments in physical units. Production of a system



synthetic spectrum involves integration over the entire (projected) system model. Software keys restrict the contributing segments to corresponding DS1 or DS2 regions. The final step is division of the integrated model intensity by the contributing model area. There are no adjustable parameters to apply to the model in a comparison with the DS1 or DS2 data. We stress that the DS1 and DS2 data are not directly observed quantities but result from MEM maps which require an assumed distance for expression in physical units.

Both data sets provide intensities for a central region that includes the WD; we have found that the most consistent overall choice for the WD  $T_{\text{eff}}$  is  $\approx 20,000\text{K}$ . Figure 3 compares our model with DS2 region ‘A’, Table 5. The error bars are an average from the Rutten et al. (1994) Table 1. The reasonably close agreement between our model and the region ‘A’ data is gratifying. Based on the error bars, the discrepancy shortward of  $5000\text{\AA}$  probably is real (i.e., not a data artifact such as, e.g., incomplete correction for atmospheric extinction at a  $2\sigma$  level) but we remain cautious in interpreting the discrepancy because of the results for Figure 4a and Figure 4b, discussed below. The discrepancy could be explained by an opacity source not included in our model.

Figure 4a compares a  $40,000\text{K}$  WD model (upper synthetic spectrum), a  $20,000\text{K}$  WD model (middle synthetic spectrum), and a zero temperature model (lower synthetic spectrum) with the G160L and prism data. The synthetic spectrum for the accretion disk contribution corresponds to BINSYN annuli 1-6. Minor corrections, not discussed here, would raise the  $40,000\text{K}$  synthetic spectrum close to the peaks of the observed spectra.

BA1998 note that there was a 70% change in  $\dot{M}$  between August 1994 (G160L) and November 1994 (prism) in the sense that the disk intensities are larger for the prism data. We empirically found that the G160L spectra accord well with the prism spectra if the G160L intensities are divided by  $1.2 \times 10^{-3}$  (and used in the plots) rather than the  $1.9 \times 10^{-3}$  factor used with the prism spectra.

The  $40,000\text{K}$  WD contributes substantially to the upper synthetic spectrum while the inner accretion disk annuli are the major contributors to the  $20,000\text{K}$  WD model; the data do not discriminate the latter model from a zero temperature WD model. (We produced the system synthetic spectrum for a zero temperature WD by suppressing the WD contribution to the integrated intensity but left the total projected area unchanged.) Note that the peak intensity for the  $20,000\text{K}$  WD model is at an ordinate value of 3.5, substantially discrepant from the peak observed intensity. The Figure 4a data are in conflict with the Figure 3 data. The WD  $T_{\text{eff}}$  is one of the principal issues to be addressed and the Figure 4a data (plus the Figure 4b data: see below) constitute the only direct evidence for a  $40,000\text{K}$  WD while the remaining data, discussed below, provide inconclusive (§6.) support for a  $20,000\text{K}$  WD.

Figure 4b shows the continuation of Figure 4a to longer wavelengths. Note the different spectral gradient at wavelengths longward of about 5500Å but possibly extending to shorter wavelengths. BA1998 describe a dropoff in the prism spectrograph response in that region and beyond while the DS2 data set (Figure 3) agrees with our model; the prism data appear to have a calibration issue (BA1998) that is insignificant at the short wavelength end but increases to longer wavelengths.

The Figure 4a error bars are small and the DS1 fractional errors gradually increase as the measured intensity drops in successive figures; to avoid excessive clutter we provide DS1 error bars only for Figure 4a and Figure 4j. Neither synthetic spectrum (the 20,000K case or the 40,000K case in Figure 4a) models the observed deep absorption features of Si II  $\lambda$ 1300; Si IV  $\lambda$ 1394, 1403; C IV  $\lambda$ 1548, 1552; He II  $\lambda$ 1640; N V  $\lambda$ 1718; Si III  $\lambda$ 1892 and Mg II  $\lambda$ 2800. It is noteworthy that the C IV  $\lambda$ 1548, 1552 doublet is in emission; Knigge & Drew (1997) show that there is a wind associated with the emission feature and that there is an underlying slow-moving ‘chromosphere’ that can produce narrow absorption reversals. The question arises whether a change in the physical conditions in the system, in the two-year interval between the Figure 3 data (obtained in 1992) and the Figure 4a data (obtained in 1994), could explain the discrepancy between the two figures. There is evidence for a high temperature source located near where a transition layer would be expected. The evidence includes a hard X-ray source (Pratt et al. 2004), an eclipsed flickering source (Bruch 2000), a 29-second oscillation source that is eclipsed (Knigge et al. 1998b), and a source of excess radiation shortward of 965Å (see below). Further discussion of the WD  $T_{\text{eff}}$  and the hot source is in §6.

Figure 4c shows the DS1 data for Table 5 radial designation 0.10. In this and subsequent plots the heavy grey line is the ‘front’ region, the light grey line is the ‘back’ region and the light continuous line is the ‘stream’. The heavy continuous line is the model synthetic spectrum. Note that the synthetic spectrum fits the DS1 data very well near 4000Å. The ‘back’ shows a higher intensity than the ‘front’ and the synthetic spectrum lies between them. At this annulus the ‘stream’ is in fair agreement with the ‘front’.

Baptista et al. discuss the lower flux levels in the ‘front’ annulus regions as compared with the ‘back’. They propose absorption due to a large number of blended lines of FeII similar to the ‘iron curtain’, hereafter IC, invoked by Horne et al. (1994), hereafter HO1994. The disk  $T_{\text{eff}}$  at this radius is about 21,000K. The IC calculated by HO1994 for OY Car (their Figure 8) produced absorption shortward of the Balmer discontinuity and increased the depth of the Balmer jump. Thus, a similar mechanism is credible to explain the ‘front’ discrepancy from the model synthetic spectrum. There is excess flux in the ‘back’ Balmer continuum, and there is no Balmer jump. Knigge et al. (1998a) propose H recombination

emission from an accretion disk chromosphere (ADC) as a mechanism to fill in the Balmer discontinuity. Their ADC is at the base of a biconical wind and has a vertical height of order  $10R_{\text{wd}}$  to provide an emission measure adequate to fill in the Balmer jump. Note the slight difference between the amount of absorption for the ‘stream’ and the ‘front’. The ADC, the IC, and the biconical wind probably are part of a single structure. The IC absorbing material most likely is located above the outer part of the accretion disk and is seen projected on the inner annuli where most of the radiative flux is produced.

The problem with the prism data calibration is apparent. If it were possible to adjust the synthetic spectrum fit empirically, the wavelength at which dropoff starts could be moved to a longer wavelength from around  $5000\text{\AA}$ . There are no adjustable parameters; it would otherwise make sense to truncate the prism spectrum at some appropriate wavelength but the fit changes from figure to figure so there is no good way to choose a truncation wavelength. These plots, including their agreement with the DS2 data (see below), serve as documentation of the prism calibration problem.

Figure 4d compares the model with prism data for radial designation 0.15. The dotted line is the data for DS2 region ‘B’. Note the agreement of the DS2 profile with the model spectrum. As in Figure 4c, the model spectrum, shortward of the Balmer limit, is intermediate between the ‘front’ and ‘back’ and is in excellent agreement with the ‘stream’. Ignoring the unmodeled emission lines, the ‘front’ Balmer jump agrees with the synthetic spectrum. The two mechanisms of Figure 4c (IC and recombination emission) also may explain the residuals here.

Figure 4e compares the model with prism data for radial designation 0.20. As in Figure 4d, shortward of the Balmer limit, the model spectrum is intermediate between the ‘front’ and ‘back’ but the ‘stream’ now lies closer to the ‘back’.

Figure 4f shows data for radial designation 0.25. The dotted line is the DS2 annulus ‘C’ spectrum. In contrast to Figure 4d, the DS2 data indicates a higher intensity than the corresponding DS1 data, while the model spectrum lies half way between the two data plots. A reduction in the model  $T_{\text{eff}}$  from the  $11,307\text{K}$  of Table 4 annulus # 19 to  $10,898\text{K}$  produces a close fit to the DS1 data longward of  $4000\text{\AA}$  and a fairly close fit shortward, consistent with a local departure from the standard model; a corresponding but smaller increase of the model  $T_{\text{eff}}$  produces a close fit to the DS2 data.

Figure 4g begins regions in the outer half of the accretion disk. The ‘stream’ here agrees well with the ‘back’, but departs increasingly in the successive regions. In Figure 4g there still is good agreement between the ‘stream’ and ‘back’. The Table 4 annulus # 23 radial position fits that of the observational data. The synthetic spectrum, with  $T_{\text{eff}} = 9855\text{K}$ , fits

the ‘back’ and ‘stream’ well shortward of  $4000\text{\AA}$  but has too large intensity on the longward side. As in Figure 4f, a reduction of the model annulus  $T_{\text{eff}}$  of a few hundred Kelvins produces a close fit to the DS1 data longward of  $4000\text{\AA}$  but interpolates half way between the ‘front’ and ‘back’ on the shortward side.

Figure 4h presents DS1 data for radial designation 0.40. The ‘stream’ intensity now exceeds that from the ‘back’ longward of  $4000\text{\AA}$  but agrees shortward of there. The synthetic spectrum is in good agreement with the prism data shortward of  $4000\text{\AA}$  and continues agreement with the ‘stream’ data to  $5000\text{\AA}$ . The ‘front’, ‘back’, and ‘stream’ now begin to show differences over much of the spectral region covered.

The dotted curve in Figure 4h is DS2 annulus ‘D’. It would compare with prism ‘.35’ data, half way between Figure 4g and Figure 4h, if those data were available. The discrepancy, in part, is due to observational data originating over a finite annular width; the hotter inner edge provides an enhanced contribution. Annulus ‘D’ closely agrees with the DS1 data of Figure 4g shortward of  $5000\text{\AA}$  but disagrees with the slope of the Figure 4g synthetic spectrum, more closely fitting the Figure 4h synthetic spectrum SED while displaced to a larger intensity. Annulus ‘D’ could be plotted either in Figure 4g or Figure 4h; for minimum congestion we have chosen Figure 4h.

Figure 4i plots DS1 data for radial region 0.50. The corresponding Table 4 annulus is # 37 with standard model  $T_{\text{eff}} = 6985\text{K}$  (inner edge), represented by the lower synthetic spectrum. DS2 annulus ‘E’ (the lower dotted line), fits the lower synthetic spectrum well. The annulus # 37 segment  $0^\circ$  to  $90^\circ$  is set to  $T_{\text{eff}} = 7500\text{K}$  and is represented by the upper synthetic spectrum. The upper dotted line is DS2 annulus ‘F’, corresponding to the same radial region as annulus ‘E’ but azimuth  $0^\circ$  to  $90^\circ$  (the ‘stream’). Since annulus ‘F’ covers a much larger radial region than the upper synthetic spectrum we do not regard the difference as serious. The (lower) standard model synthetic spectrum agrees well with the ‘back’; its representative point, at  $\log r/r_{\text{L1}} = -0.3$ , Figure 1, falls on the dotted line below the observed data points. The higher temperature annular segment falls on the Figure 1 heavy continuous curve passing through the region of observed points.

Figure 4j shows DS1 data for radial region 0.60. The corresponding Table 4 annulus is # 44,  $T_{\text{eff}} = 6158\text{K}$  (inner edge). The lower heavy line is that model. To represent the ‘stream’ we have reset the annulus # 44  $T_{\text{eff}}$ , between azimuth  $0^\circ$  and  $90^\circ$ , to  $8600\text{K}$ . The upper synthetic spectrum represents that annular segment. The DS1 ‘stream’ and ‘back’ agree shortward of  $4000\text{\AA}$  but the very large ‘stream’ Balmer jump is larger than the synthetic spectrum represents. The differences between the ‘front’ and ‘back’ are close to their errors and we do not regard their differences or their departure from the synthetic spectrum as significant. Note the change in ordinate scales from Figure 4a to Figure 4j; the intensity

values change by roughly a factor 50.

We have interpolated  $T_{\text{eff}}$  values for the azimuth  $0^\circ$  to  $90^\circ$  segments at annuli between # 30 and # 44 where the ‘stream’ differs significantly from the ‘back’. This completes our accretion disk model and prepares a comparison with other data sets.

#### 4.1. Light curve simulations

We simulate *UBV* light curves via synthetic photometry. We calculated synthetic system spectra at 81 orbital phases, distributed to cover the variable parts of the light curve with adequate phase resolution. The synthetic spectra were based on the intensity version of SYNSPEC, which provides automatic wavelength-dependent correction for limb darkening, but converted to flux-based spectra for the final output. Each synthetic spectrum was weighted by the pass bands for the V,B, and U standard filters and the products integrated. The integrated flux in V,B, and U, normalized to the flux maxima, as function of phase constitute the theoretical light curves.

The software represents the bright spot as a rim section of elevated  $T_{\text{eff}}$  (Wood et al. 1986, 1989); this is a modification of the (otherwise) isothermal rim (§3.1). The bright spot covers the full rim height; the structure of our present program does not allow a variable rim thickness with azimuth. The rim semi-thickness,  $H$ , Table 2, follows from the standard model (Frank, King, & Raine 1992, eq.5.39). It was necessary to assign the region of elevated temperature to an extended azimuth region on the rim, in agreement with Smak (1994a), to fit the Walker & Herbig (1954) observations (see Table 6 for the spot parameters). Hydrodynamical 2D models of the stream impact Różyczka (1985, 1988) identify two shock waves: (1) a shock on a plane perpendicular to the orbital plane, roughly bisecting the angle between the stream and the rim and terminating at the upstream edge of the stream, and (2) a shock slightly more inclined to the stream and extending far into the disk. Although the simulation is 2D, Różyczka (1985) states that a bow shock will develop, prospectively leading to vertical expansion upstream. Livio, Soker, & Dgani (1986) and Armitage & Livio (1998) perform a 3D simulation and find that material from the stream flows over the disk if cooling is efficient, applicable to low  $\dot{M}$  cases, and is more like an explosion in high  $\dot{M}$  cases, leading to a bulge extending along the disk rim. The inclined shock wave plane suggests that a more complex model would provide a better physical representation of the bright spot than adopted in this study. HO1994 developed a model of this type in their study of OY Car, in contrast to the ‘painted on’ rim model of Wood et al. (1989) for the same star.

Figure 5 shows the fit to the *V* light curve, Figure 6 shows the fit to the *B* light curve,

and Figure 7 shows the fit to the  $U$  light curve with a depth residual. A  $U$  eclipse depth residual, differing from the good  $V$  and  $B$  fits, is suggestively familiar from the binary star literature; it results from the poor representation of stellar SEDs by a black body over the Balmer discontinuity. That explanation is not possible here since the synthetic spectra simulate the Balmer discontinuity. The far edge of the accretion disk remains uneclipsed and it is this region that shows extra unmodeled light shortward of the Balmer discontinuity (Figure 4). We suggest that it is this unmodeled, uneclipsed light that reduces the observed depth of  $U$  eclipse below the model. These light curves adopt a 20,000K WD as discussed in the previous section. The eclipse depths are more strongly correlated with orbital inclination than WD  $T_{\text{eff}}$  and so are not useful in distinguishing between a 20,000K WD and a 40,000K WD. We call attention to the downward trend in the Figure 6 residuals between orbital phases 0.2 and 0.8. §6 discusses this feature in terms of a vertically extended rim. It is of interest that the model provides a good light curve fit over the range of dates from April 17, 1953 ( $B$ ) to June 13, 1953 ( $U$ ).

We have tested the sensitivity of our model to our choice of  $R_{\text{cutoff}} = 0.6R_{\text{L1}}$  by setting  $R_{\text{cutoff}} = 0.7R_{\text{L1}}$  and recalculating the model light curves. The eclipse widths remain the same to visual detectability limits while the eclipse depths become systematically smaller by small amounts; the  $U$  calculated depth now fits the observations precisely while the  $V$  and  $B$  calculated depths are slightly too shallow.

## 5. SED fits to observed spectra

We apply the model developed in previous sections, including the rim bright spot from the immediately previous section, hereafter the §4. model, to represent observed spectra. The SYNSPEC synthetic spectra for the annuli of Table 3 are produced in both an intensity format and a flux-based format; the latter format requires adoption of a wavelength-independent limb darkening coefficient. The intensity simulations of §4 required the intensity-based synthetic spectra. We used the intensity-based synthetic spectra, which automatically correct for wavelength-dependent limb darkening, and converted the output to flux units for comparison with the observed spectra which are tabulated in physical flux units.

### 5.1. SED fits to *FUSE* and *FOS* spectra

The *FOS* spectra have already been used by BA1998 to produce the MEM data modeled in Figure 4. Our objective in this section is to combine the *FOS* and *FUSE* spectra and

model those observed spectra. The *FOS* and *FUSE* spectra have exposure times listed in Table 1. *FUSE* orbit03 exposure starts at orbital phase 0.4333 and ends at 0.5117. *FUSE* orbit04 exposure starts at orbital phase 0.7863 and ends at orbital phase 0.8750. Both of the *FUSE* exposures start and end outside eclipse. The first G160L exposure, data set Y2AH0201T, starts at orbital phase  $-0.090$  and ends at orbital phase 0.130. The second G160L exposure, data set Y2AH0401T, starts at orbital phase  $-0.063$  and ends at orbital phase 0.156. As BA1998 indicate, in each case the *FOS* data set consists of 691 spectra produced in ‘rapid readout’ mode. In each *FOS* case, our spectrum is the sum of the exposures in the data set.

To simulate the sum of the exposures for the *FOS* spectra, we calculated 33 synthetic system spectra equally spaced in phase between phase  $-0.063$  and 0.156, corresponding to the Y2AH0401T data set. These spectra all used a 20,000K model for the WD, specifically for  $\dot{M} = 5.0 \times 10^{-9} M_{\odot} \text{ yr}^{-1}$ . BA1998 note that there was a 70% reduction in  $\dot{M}$  from the DS1 observations to the *FOS* observations. Experiment shows that a change like this does not make a large change in the calculated spectral gradient; the major change is in the flux level. Rather than calculate a complete new set of TLUSTY annuli and a corresponding new BINSYN model, we preserve the adopted  $\dot{M}$  and subsume the effect of the  $\dot{M}$  change in the normalization factor to superpose the model on the observed spectra (see below). We summed the spectra and divided by 33 to produce an average spectrum through eclipse. Comparison of the average spectrum with one that is outside eclipse shows that the average spectrum closely fits the outside-eclipse profile but has a flux level that is 88% of the outside-eclipse spectrum. We use this average spectrum for comparison with both of the *FOS* spectra.

Figure 8 compares two synthetic spectra with the YAH0201T spectrum. The lower synthetic spectrum is the average spectrum described above and the upper synthetic spectrum is the 40,000K model. It is apparent that the synthetic spectrum departs significantly from the observed spectrum. In the following section we will find that the same is true of the *IUE* spectra and that the SED is appreciably variable, temporally, with  $T_{\text{eff}}$  profiles that differ from the standard model. A fair overall fit can be achieved shortward of  $2100 \text{ \AA}$  with a normalizing factor of  $7.5 \times 10^{41}$ , corresponding to a distance of 281pc. This distance is too large because of the failure to allow for the reduced  $\dot{M}$  described above. A correction moves the calculated distance toward the adopted 250pc. The 40,000K WD model shown (calculated for an outside-eclipse phase), with the same normalizing factor, lies well above the observed spectrum and would require a larger normalizing factor to fit the observed spectrum. Reducing to 88% of the calculated flux to allow for effects of eclipse still leaves a large discrepancy.

A completely self-consistent loop for the §4. model would determine a normalizing factor that reproduces the assumed initial model distance of 250pc. Note that this analysis, while adopting values of  $M_{\text{wd}}$  and  $\dot{M}$ , leaves the distance as a parameter to be determined. By contrast, in Figure 4, the data to be fit involve an assumed distance but there is no adjustable parameter in the comparison with the model.

Figure 9 presents the FUV spectrum for the Figure 8 configuration. The *FUSE* spectrum is outside eclipse so the synthetic spectrum for the 20,000K model also represents that condition, as does the 40,000K synthetic spectrum. The §4. model (lower synthetic spectrum) fits the *FUSE* spectrum approximately but does not reproduce the very large number of fairly deep absorption features. The absorption features in the 1120Å to 1150Å region of the synthetic spectrum are replicated with much larger amplitude in the *FUSE* spectrum. FR2003 discuss the *FUSE* spectra in detail. Reddening has a strong effect; a change from  $E(B-V)=0.00$  to  $E(B-V)=0.01$  raises the *FUSE* spectrum by 17% without a detectable change in the slope. The reddening-corrected spectrum fits the synthetic spectrum better but, as noted below, the *FUSE* spectrum shows phase-wise variation that makes the value of the fit questionable. We do not consider the improved fit necessarily as support for a value of  $E(B-V)=0.01$ . Note that the emission excess shortward of 965Å, described by FR2003, is clearly present. Also note the blueward displacement of the  $\text{Ly}\beta$  and  $\text{Ly}\gamma$  absorption features; the model approximately reproduces their depths. The corresponding Doppler shift is  $\sim 3000 \text{ km s}^{-1}$ .

Figure 10 combines the G160L spectrum from the Y2AH0401T set with the *FUSE* orbit04 spectrum (the phase of the *FUSE* spectrum is unrelated to the phase of the G160L spectrum; they have been plotted together for economy—otherwise separate plots would be required). Because of the same total phase range for the two *FOS* spectra and the same number of contributing individual spectra they would be expected to be essentially identical. Yet the G160L spectrum shows an overall flux reduction, is substantially fainter in the 1200Å to 1500Å region, but now shows an excellent fit longward of 2000Å. The accretion disk SED has changed between the times of the two observation sets.

Figure 11, which shows the FUV part of Figure 10, poses a problem. As with Figure 9, the 20,000K model represents an outside-eclipse phase. The *FUSE* spectrum is outside eclipse so it would be expected to show little difference from Figure 9, yet the difference is striking. Not only is the flux level lower, there appear to be absorption bands that are not prominent in Figure 9. Note the broader, deeper and more complex  $\text{Ly}\beta$  and  $\text{Ly}\gamma$  features, but the emission excess shortward of 965Å is unaffected. The *FUSE* spectrum shows variation which may be both/either temporal or phase-dependent.



## 5.2. SED fits to *IUE* spectra

The *IUE* archive lists 31 LWP and LWR spectra, and 37 SWP spectra, mostly observed in 1980 and mostly taken in pairs including a LWR exposure and a SWP exposure. We used the BA1995 ephemeris  $T_{\min} = \text{HJD } 2443904.87872 + 0.196671278E$  to calculate orbital phases. The UX UMa orbital period is short enough, and the *IUE* exposure time long enough, that the second exposure of a pair occurred at an orbital phase differing appreciably from the first. For example, in the pair SWP10128+LWR08799 the first exposure started at orbital phase 0.2887 while the second started at 0.4069. In cases where both exposures are outside eclipse the phase displacement between exposures makes an undetectable change in the synthetic spectra; consequently we combine the observed spectra of a pair for analysis. Separate tests with outside-eclipse synthetic spectra show nearly undetectable phase-wise variation in the SED even though the model includes the rim bright spot. The observed spectra do show cycle to cycle changes and there are year to year changes that are clearly apparent (Holm, Panek, & Schiffer 1982) (see below). We find that our model with a 20,000K WD provides an appreciably better fit, in all cases tested, than a 40,000K WD. A 40,000K WD produces a too-steep spectral gradient (see below).

Figure 12 presents a fit to SWP10371+LWR09051. The orbital phase at the start of the SWP exposure was 0.2867 and the phase at the start of the LWR exposure was 0.1615. Both exposures were outside eclipse. The synthetic spectrum has been divided by  $5.2 \times 10^{41}$  for this comparison, showing a reasonably close fit to the *IUE* spectra except beyond 2600Å; the corresponding distance is 234pc. This fit appears to provide support for our adopted distance of 250pc, but, as we see in the following discussion, the support is ambiguous. The upturn at 2600Å is not due to the secondary star since BINSYN includes an explicit model of the secondary star in the simulation; this effect mimics the Figure 8 anomaly. Plots of the *IUE* spectra and the G160L plus prism spectra show a substantially different flux level in the two cases, indicating a likely change in  $\dot{M}$  between the times of observation. (The *IUE* 1350Å continuum flux in Figure 12 is about 3.0 ordinate units while the corresponding level in Figure 8 is about 2.2 ordinate units.)

Figure 13 presents a fit to SWP10128+LWR08798. The orbital phase at the start of the SWP exposure was 0.2887 and the phase at the start of the LWR exposure was 0.4069. The synthetic spectrum has been divided by  $5.2 \times 10^{41}$ , as in Figure 12. The discrepancy beyond 2600Å in Figure 12 now afflicts Figure 13 beyond 1700Å. A possible postulate to explain Figure 13 is a lower accretion disk temperature gradient. The required change is drastic: A 20,000K WD and a 12,000K isothermal accretion disk provide a good fit, with a normalizing factor of  $3.5 \times 10^{41}$ , placing the system at a distance of 192pc. But the excess radiation above the synthetic spectrum with the Figure 12 normalizing factor, nearly

consistent with the adopted distance of UX UMa, indicates an actual *increase* in total disk luminosity, contradicting the implication of the reduced normalizing divisor. Thus, the isothermal accretion disk model fits the *IUE* spectrum but does not provide a believable system model.

Finally, Figure 14 presents a fit to SWP10677+LWR09388. This spectrum permits an excellent fit by a standard model, but with a mass transfer rate of  $\dot{M} = 3.0 \times 10^{-9} M_{\odot} \text{ yr}^{-1}$ ; the corresponding distance is 165pc. The actual mass transfer rate in UX UMa may, at times, equal the value quoted, but if the accretion disk reaches equilibrium, the flux values will differ appreciably from the Figure 14 values.

Our conclusions from simulation of these and other *IUE* spectra are: (1) The Figure 8 anomaly occurs frequently but may start at shorter or longer wavelengths than 2000Å. The source of the anomaly is unknown. (2) In some cases, the SED in a variable  $\dot{M}$  system can be accurately fit by a nonstandard model (e.g., isothermal) that does not lead to a believable system model; the fit cannot be used even to constrain the disk luminosity. (3) As a caution to disk modelers, a good standard model fit in a system that shows spectrum variability cannot be taken at face value, even if the  $\dot{M}$  indicates that the accretion disk is stable against outburst, unless there is independent evidence concerning the system distance.

## 6. Discussion

An important part of the system analysis for UX UMa depends on knowledge of its distance. BA1995 calculate a value of 345pc with an estimated error of 34pc. The 345pc determination depends on fits in a color-magnitude diagram, with one wavelength at 1523Å. The fits use a theoretical color-magnitude relation derived on assumed radiation characteristics of the source. If the source can be represented by a black body, the derived distance is 401pc, and if standard Kurucz model atmospheres, 312pc. We feel the residuals in the SED fits found in the present study are large enough that an assumed radiation characteristic for the source should be treated with caution, and that the estimated error in the 345pc determination could be larger. Other distance determinations are in §3. The Knigge (2006) method is an important improvement on the Bailey (1981) relation; as cited in §3., this method leads to a distance of 215pc if the secondary provides all of the system K-flux and 376pc if the secondary provides 1/3 of the system flux. Based on the parameters of our §4. model, and adopting a secondary  $T_{\text{eff}} = 3575\text{K}$  (Knigge 2006, Table 3) the secondary provides 0.48 of the system flux at  $2.2\mu$ , leading to a calculated distance of 312pc. Consider the sensitivity of the calculated distance to variation of system parameters. The flux ratio secondary/(secondary+disk) is sensitive to the accretion disk flux which in turn depends

on  $\dot{M}$ . (The contribution of the adopted 20,000K WD is only a few tenths of a percent at  $2.2\mu$ .) From Figure 1 we estimate that the scatter of the observational data constrains  $\dot{M}$  within a factor of about 2 for the adopted system distance of 250pc. Increasing  $\dot{M}$  to  $1.0 \times 10^{-8} M_{\odot} \text{ yr}^{-1}$  produced a new calculated distance of 332pc. We increased  $M_{\text{wd}}$  by 10%, while maintaining  $M_{\text{sec}}$  fixed, to test the calculated distance sensitivity to  $M_{\text{wd}}$  variation. The new distance was 323pc. Variation in the observed K magnitude of a few times 0.01 produces variation of only a few parsecs in the calculated distance. We propose a distance of  $312 \pm 30$ pc as the best currently available distance determination to UX UMa and note the accordance with the value found by BA1995 using a fit to Kurucz model atmospheres.

This study finds that a standard model  $\dot{M} = 5.0 \times 10^{-9} M_{\odot} \text{ yr}^{-1}$  accretion disk surrounding a 20,000K (but see below),  $0.47 M_{\odot}$  WD at a distance of 250pc provides a model that reasonably fits spectral intensity data (Figure 4) and spectral flux data (Figure 8 through Figure 11). All of the DS1 and DS2 data can be equally well represented if the distance is 345pc and  $\dot{M} = 1.0 \times 10^{-8} M_{\odot} \text{ yr}^{-1}$ . In particular, the observational data of Figure 1 depend only on the adopted distance. Interpolating between the 250pc and 345pc calibrations, for our preferred distance of 312pc, the corresponding  $\dot{M} = 8 \times 10^{-9} M_{\odot} \text{ yr}^{-1}$ . We take this value to be our final result for the mass transfer rate. In principle it would be possible to iterate our solution, starting over with the new distance and  $\dot{M}$  determination but, based on our study of the  $\dot{M} = 1.0 \times 10^{-8} M_{\odot} \text{ yr}^{-1}$  case at 345pc, we believe there would be no improvement in any of the plots presented in this paper.

Puebla et al. (2007) (hereafter P2007) use a separate method to study accretion rates and, for UX UMa (their Table 2) find  $\dot{M} = 1.7 \times 10^{-8} M_{\odot} \text{ yr}^{-1}$  from black body fits and  $\dot{M} = 1.4 \times 10^{-8} M_{\odot} \text{ yr}^{-1}$  for their model accretion disk fits, adopting a distance to UX UMa of 340pc and  $M_{\text{wd}}/M_{\odot}$  in the range 0.4-0.8. This result is in approximate agreement with our results. In their Figure 6 P2007 fit *IUE* spectra of UX UMa with two models. Their second model, for  $M_{\text{wd}}/M_{\odot} = 0.4$ , finds  $\dot{M} = 5.5 \times 10^{-9} M_{\odot} \text{ yr}^{-1}$ , in close agreement with our model. P2007 parameterize the WD contribution with  $\zeta = f_{\text{wd}}/f_{\text{disk}}$  and define a “disk-dominated” system as one in which  $\zeta < 0.1$ , where the flux values are integrated contributions from 1500Å to 3250Å. We would prefer to define “disk-dominated” in terms of an integration extending to 950Å since a large part of the flux from a hot WD can occur shortward of 1500Å. Because of the ambiguity of the WD  $T_{\text{eff}}$  in UX UMa (see below), we do not estimate a value for  $\zeta$  except to note that, from Figure 4a, the accretion disk supplies well over 90% of the system flux if the WD  $T_{\text{eff}} = 20,000\text{K}$  (compare with the zero temperature WD where the accretion disk supplies 100% of the system flux, excluding the secondary).

Several studies (§3) support the adopted  $M_{\text{sec}} = 0.47 M_{\odot}$ . The adoption of  $q = 1.0$  places the system at the boundary of instability against dynamical scale mass transfer and

a  $M_{\text{wd}}$  larger than  $0.47M_{\odot}$  seems likely. Baptista et al. (1995) state that adoption of the Smak (1994a)  $M_{\text{wd}} = 0.70M_{\odot}$  increases the system distance from 345pc to 386pc; the effect of a smaller  $q$  is to increase the size of the accretion disk and so make it more luminous. A WD mass greater than  $0.47M_{\odot}$  would be smaller and would produce a deeper potential well so, for the same  $\dot{M}$ , the accretion disk would be hotter and the spectral gradient would be steeper. Preservation of a fit to the calibrated temperatures of Figure 1 would require either a reduction in  $\dot{M}$  or a nonstandard model temperature profile.

The evidence concerning the WD  $T_{\text{eff}}$  is ambiguous. BINSYN requires specification of a WD  $T_{\text{eff}}$  and our adopted §4. model includes a 20,000K WD but, as Figure 4a shows, this model differs almost negligibly from a zero temperature WD; the hotter inner annuli, Table 4, contributions dominate the system synthetic spectrum. A 40,000K or hotter WD, directly visible to the observer, would be strongly inconsistent with the Figure 3 intensity data while the SED data, Figure 8 through Figure 11, all are inconsistent with a hot WD. The only data supporting a hot WD are Figure 4a and Figure 4b. Although the DS1 data plotted in Figure 4a and Figure 4b superficially support a 40,000K WD, we find it more attractive to attribute the excess flux source to something like a boundary layer in common with the other unmodeled hot sources described in connection with Figure 4a. We argue that, in Figure 4a, the central region is seen through an absorbing layer, likely the “transition region” between the accretion disk and the fast wind (Knigge & Drew 1997), which produces the deep absorption features.

Studies of other cataclysmic variable systems generally support a WD  $T_{\text{eff}}$  hotter than 34,000K (Sion 1999; Knigge et al. 2000; Sion et al. 2008) at the orbital period of UX UMa. It is informative that the WD temperature determination for DW UMa obtained during a low state of accretion when the WD was clearly visible (Knigge et al. 2000) were much higher than during the normal high accretion state, indicating that the accretion disk can occult the WD. Since the orbital period of UX UMa is outside the range for systems that undergo low states, there is no opportunity to determine how much disk occultation occurs. Sion (1999, Table 3) lists CV systems for which absorbing curtains obscuring the WDs have been calculated. Note that our application would be more complex since, in addition to obscuring the central region, we require obscuration of the ‘front’ of particular annular regions, separate from the WD.

As we have demonstrated, an accretion disk with constant  $\dot{M}$  fits both the DS2 and DS1 observations, and this datum (a fixed, unchanging accretion disk) might imply that a changed WD explains the difference between Figure 3 and Figure 4b. But if  $\dot{M}$  has remained nearly constant we see no mechanism to heat the WD (and we do not believe a changed  $\dot{M}$  could heat the WD from 20,000K to 40,000K), while there are documented changes in the

accretion disk (Figure 8 to Figure 13) and one such change might be formation of a hot emitting region between the times of the two data sets (June 4, 6, and 7, 1992 for DS2 and Nov. 11, 1994 for DS1).

Our relatively simple bright spot model, §4.1, represents the *UBV* light curves of Figure 5 through Figure 7, including the luminosity maximum just before eclipse. These simulations are the basis for our determination of the system orbital inclination. UX UMa occasionally shows anomalous light curves that can not be represented by even a sophisticated model like that of HO1994. An example is in Figure 15. Less extreme cases show a depressed light level from phase 0.2 to 0.8, with a downward tilt to phase 0.8, followed by a rapid rise to light maximum at phase 0.9. These features become more pronounced from *V* to *B* to *U*. An example is (our) Figure 6 or Figure 3 of Johnson, Perkins, & Hiltner (1954). Mason, Drew, & Knigge (1997) attribute this effect to a disk ‘bulge’ upstream from the bright spot and tie it to a similar effect in UV spectra. In Figure 15 we suggest that, except for a temporally enlarged ‘bulge’ or associated disturbance, the system would show a brightness peak at orbital phase 0.9 with a brightness reduction to the light level seen at phase 0.15. The same ‘dips’ are seen in LMXRBs, discussed by Livio (1993) and with the same proposed explanation. This subject is discussed further by Knigge et al. (1998a) and FR2003. This explanation for anomalous light curves differs from the Smak (1994b) proposal for circumdisk absorbing material.

An important result of this study is that, starting with an adopted distance of 250pc to UX UMa, intensity-based observed spectra, flux-based observed spectra, and photometric data all can be approximately represented by a standard model with  $\dot{M} = 5.0 \times 10^{-9} M_{\odot} \text{ yr}^{-1}$  and with an elevated temperature in the accretion disk quadrant that includes the stream impact region. Application of the Knigge (2006) method then leads to an improved distance estimate of 312pc followed by a revised estimate of the (average) mass transfer rate (at the times of the DS1 and DS2 data sets). In spite of this success, SED fits show departures from the standard model in agreement with BINSYN studies of IX Vel (Linnell et al. 2007) and QU Car (Linnell et al. 2008) which also exhibit departures from a standard model. We postpone attempting to model the IC and the recombination spectrum that fills in the Balmer continuum for the ‘back’ spectra, Figure 4c to Figure 4j, to a subsequent publication.

We thank the referee for a prompt report; responding to it substantially improved this paper. We are grateful to Dr. Baptista for supplying data from BA1998 for this investigation. PG wishes to thank Mario Livio for his kind hospitality at the Space Telescope Science Institute where part of thi work was carried out. Support for this work was provided by NASA through grant number HST-AR-10657.01-A to Villanova University (P. Godon) from the Space Telescope Science Institute, which is operated by the Association of Universities for

Research in Astronomy, Incorporated, under NASA contact NAS5-26555. PS is supported by HST grant GO-09724.06A.

This research was partly based on observations made with the NASA/ESA Hubble Space Telescope, obtained at the Space Telescope Science Institute, which is operated by the Association of Universities for Research in Astronomy, Inc. under NASA contract NAS5-26555, and the NASA-CNES-CSA *Far Ultraviolet Explorer*, which is operated for NASA by the Johns Hopkins University under NASA contract NAS5-32985.

## REFERENCES

- Armitage, P. J., & Livio, M. 1998, ApJ, 493, 898
- Bailey, J. 1981, MNRAS, 197, 31
- Baptista, R., Horne, K., Hilditch, R. W., Mason, K. O., & Drew, J. E. 1995, ApJ, 448, 395 (BA1995)
- Baptista, R., Horne, K., Wade, R. A., Hubeny, I., Long, K. S., & Rutten, R. G. M. 1998, MNRAS, 298, 1079 (BA1998)
- Becker, R. H. 1981, ApJ, 251, 626
- Bruch, A. 2000, A&A, 359, 998
- Bruch, A., & Engel, A. 1994, A&AS, 104, 79
- Frank, J., King, A. R., Sherrington, M. R., Jameson, R. F., & Axon, D. J. 1981, MNRAS, 195, 505
- Frank, J., King, A., & Raine, D. 1992, *Accretion Power in Astrophysics* (Cambridge: Univ. Press)
- Froning, C. S., Long, K. S., & Knigge, C. 2003, ApJ, 584, 433 (FR2003)
- Holm, A. V., Panek, R. J., & Schiffer, F. H., III 1982, ApJ, 252, L35
- Horne, K., Marsh, T. R., Cheng, F.-H., Hubeny, I., & Lanz, T., 1994, ApJ, 426, 294 (HO1994)
- Hubeny, I. 1988, Comp. Phys. Comm., 52, 103
- Hubeny, I. 1990, ApJ, 351, 632

- Hubeny, I., Lanz, T., & Jeffery, C. S. 1994, in Newsletter on Analysis of Astronomical Spectra No. 20, ed. C. S. Jeffery (CCP7;St. Andrews: St. Andrews Univ.), 30
- Hubeny, I., & Lanz, T. 1995, ApJ, 439, 875
- Hubeny, I., & Hubeny, V. 1998, ApJ, 505, 558
- Johnson, H. L., Perkins, B., & Hiltner, W. A. 1954, ApJS, 1, 91
- King, A. R., Frank, J., Jameson, R. F., & Sherrington, M. R. 1983, MNRAS, 203, 677
- Knigge, C., 2006, MNRAS, 373, 484
- Knigge, C., & Drew, J. E. 1997, ApJ, 486, 445
- Knigge, C., Long, K. S., Wade, R. A., Baptista, R., Horne, K., Hubeny, I., & Rutten, R. G. M. 1998, ApJ, 499, 414
- Knigge, C., Drake, N., Long, K. S., Wade, R. A., Horne, K., & Baptista, R. 1998, ApJ, 499, 429
- Knigge, C., Long, K. S., Hoard, D. W., Szkody, P., & Dhillon, V. S. 2000, ApJ, 539, L49
- Krzemiński, W., & Walker, M. F. 1963, ApJ, 138, 146
- Linnell, A. P., & Hubeny, I. 1996, ApJ, 471, 958
- Linnell, A. P., Godon, P., Hubeny, I., Sion, E. M., & Szkody, P. 2007, ApJ, 662, 1204
- Linnell, A. P., Godon, P., Hubeny, I., Sion, E. M., Szkody, P., & Barrett, P. 2008, ApJ, 676, 1266
- Livio, M. 1993, in Accretion Disks in Compact Stellar Systems ed. J. Craig Wheeler (Singapore:World Scientific), p.243
- Livio, M., Soker, N., & Dgani, R. 1986, ApJ, 305, 267
- Mason, K. O., Drew, J. E., Córdova, F. A., Horne, K., Hilditch, R., Knigge, C., Lanz, T., & Meylan, T. 1995, MNRAS, 274, 271
- Mason, K. O., Drew, J. E., & Knigge, C. 1997, MNRAS, 290, L23
- Nather, R. E., & Robinson, E. L. 1974, ApJ, 190, 637
- Osaki, Y. 1996, PASP, 108, 39

- Panei, J. A., Althaus, L. G., & Benvenuto, O. G. 2000, *A&A*, 353, 970
- Pratt, G. W., Mukai, K., Hassall, B. J. M., Naylor, T., & Wood, J. H. 2004, *MNRAS*, 348, L49
- Puebla, R., Diaz, M., & Hubeny, I. 2007, *AJ*, 134, 1923 (P2007)
- Różyczka, M. & Schwarzenberg-Czerny, A. 1987, *Acta Astr.*, 37, 141
- Różyczka, M. 1988, *Acta Astr.*, 38, 175
- Rutten, R. G. M., van Paradijs, J., & Tinbergen, J. 1992, *A&A*, 260, 213
- Rutten, R. G. M., Dhillon, V. S., Horne, K., & Kuulkers, E. 1994, *A&A*, 283, 441
- Schlegel, E. M., Honeycutt, R. K., & Kaitchuck, R. H. 1983, *ApJS*, 53, 397
- Shafter, A. W. 1984, *AJ*, 89, 1555
- Shakura, N. I., & Sunyaev, R. A. 1973, *A&A*, 24, 337
- Sion, E. M. 1999, *PASP*, 111, 532
- Sion, E. M., Gänsicke, B. T., Long, K. S., Szkody, P., Knigge, C., Hubeny, I., DeMartino, D., & Godon, P. 2008, *ApJ*, 681, 543
- Smak, J. 1994a, *Acta Astron.*, 44, 59
- Smak, J. 1994b, *Acta Astron.*, 44, 257
- Smak, J. 2002, *Acta Astron.*, 52, 263
- Walker, M. F., & Herbig, G. H. 1954, *ApJ*, 120, 278
- Warner, B. 1995, *Cataclysmic Variable Stars* (Cambridge: Cambridge University Press)
- Wood, J. H., Horne, K., Berriman, G., Wade, R., O'Donoghue, D., & Warner, B. 1986, 219, 629
- Wood, J. H., Horne, K., Berriman, G., & Wade, R. A. 1989, *ApJ*, 341, 974
- Wood, J. H., Naylor, T., & Marsh, T. R. 1995, *MNRAS*, 274, 31



Table 1. Spectroscopic observations of UX UMa

Date (dd/mm/yyyy)	Telescope Instrument	Exp time (sec)	Orb. Phase	Dataset
14-09-1980	IUE	1680	0.2887	SWP10128
14-09-1980	IUE	1800	0.4069	LWR08799
16-10-1980	IUE	1800	0.2867	SWP10371
16-10-1980	IUE	1800	0.1615	LWR09051
25-11-1980	IUE	2699	0.3050	SWP10677
25-11-1980	IUE	1800	0.4936	LWR09388
03-08-1994	FOS(G160L)	3581	0.9109	Y2AH0201T
03-08-1994	FOS(G160L)	3581	0.9368	Y2AH0401T
24-11-1994	FOS(PRISM)	4509	0.8383	Y2AH0601T
24-11-1994	FOS(PRISM)	4509	0.8807	Y2AH0801T
24-03-2001	FUSE	1332(orbit 3)	0.4333	B08201010
24-03-2001	FUSE	1508(orbit 4)	0.7863	B08201010

Note. — The listings in the orbital phase column refer to the start of the exposures

Table 2. UX UMa Model System Parameters,  $M_{\text{wd}} = 0.47M_{\odot}$

parameter	value	parameter	value
$M_{\text{wd}}$	$0.47M_{\odot}$	$r_s(\text{pole})$	$0.496R_{\odot}$
$M_s$	$0.47M_{\odot}$	$r_s(\text{point})$	$0.697R_{\odot}$
P	0.196671278 days	$r_s(\text{side})$	$0.521R_{\odot}$
$D$	$1.39345R_{\odot}$	$r_s(\text{back})$	$0.564R_{\odot}$
$\Omega_{\text{wd}}$	85.4	$\log g_s(\text{pole})$	4.73
$\Omega_s$	3.75	$\log g_s(\text{point})$	-4.65
$i$	$70.2 \pm 0.2^{\circ}$	$\log g_s(\text{side})$	4.65
$T_{\text{eff,wd}}$	20,000K <sup>a</sup>	$\log g_s(\text{back})$	4.50
$r_{\text{wd}}$	$0.0165R_{\odot}$	$r_a$	$0.488R_{\odot}$
$\log g_{\text{wd}}$	7.7	$r_b$	$0.0165R_{\odot}$
		$H$	$0.0158R_{\odot}$

<sup>a</sup>see text for discussion

Note. — wd refers to the WD;  $s$  refers to the secondary star.  $D$  is the component separation of centers,  $\Omega$  is a Roche potential.  $r_a$  specifies the outer radius of the accretion disk, set at the tidal cut-off radius, and  $r_b$  is the accretion disk inner radius.  $H$  is the semi-height of the accretion disk rim (standard model).

Table 3. Properties of accretion disk with mass transfer rate  $\dot{M} = 5.0 \times 10^{-9} M_{\odot} \text{yr}^{-1}$  and WD mass of  $0.47 M_{\odot}$ .

$r/r_{\text{wd},0}$	$T_{\text{eff}}$	$m_0$	$T_c$	$\log g$	$z_H$	$\tau_{\text{Ross}}$
1.36	39724	1.256E4	4.341E5	6.55	1.35E8	3.48E4
2.00	35617	1.534E4	4.081E5	6.29	2.34E8	4.18E4
3.00	28801	1.499E4	3.504E5	6.00	4.08E8	5.25E4
4.00	24207	1.395E4	3.102E5	5.78	5.86E8	6.40E4
5.00	20997	1.296E4	2.815E5	5.61	7.71E8	7.63E4
6.00	18628	1.210E4	2.602E5	5.47	9.67E8	8.95E4
7.00	16803	1.137E4	2.431E5	5.35	1.16E9	1.03E5
8.00	15349	1.074E4	2.291E5	5.25	1.37E9	1.17E5
9.00	14159	1.019E4	2.167E5	5.16	1.57E9	1.29E5
10.00	13167	9.714E3	2.058E5	5.07	1.79E9	1.41E5
12.00	11598	8.916E3	1.857E5	4.93	2.21E9	1.57E5
14.00	10409	8.274E3	1.622E5	4.79	2.55E9	1.54E5
16.00	9472	7.745E3	1.466E5	4.67	2.84E9	1.51E5
20.00	8082	6.916E3	1.233E5	4.65	6.97E9	1.39E5
24.00	7093	6.929E3	1.076E5	4.35	4.77E9	1.32E5
30.00	6040	5.593E3	0.936E5	4.13	5.51E9	1.42E5

Note. — Each line in the table represents a separate annulus. A Shakura & Sunyaev (1973) viscosity parameter  $\alpha = 0.1$  was used in calculating all annuli.  $r_{\text{wd},0}$  is the radius of a zero temperature, carbon, Hamada-Salpeter WD. See the text for additional comments.

Table 4. BINSYN model accretion disk with mass transfer rate  $\dot{M} = 5.0 \times 10^{-9} M_{\odot} \text{yr}^{-1}$  and WD mass of  $0.47 M_{\odot}$ .

ordinal val.	r/r <sub>wd</sub>	r/r <sub>L1</sub>	T <sub>eff</sub>	ordinal val.	r/r <sub>wd</sub>	r/r <sub>L1</sub>	T <sub>eff</sub>
1	1.0000	.02370	33896.	24	13.3394	.31610	9557.
2	1.1806	.02798	33896.	25	13.9098	.32962	9280.
3	1.3611	.03225	35256.	26	14.4802	.34313	9021.
4	1.9315	.04577	32098.	27	15.0506	.35665	8778.
5	2.5019	.05929	28289.	28	15.6210	.37017	8550.
6	3.0723	.07280	25210.	29	16.1914	.38368	8336.
7	3.6427	.08632	22765.	30	16.7618	.39720	8134.
8	4.2131	.09984	20795.	31	17.3322	.41072	7943.
9	4.7835	.11353	19177.	32	17.9026	.42423	7762.
10	5.3539	.12687	17823.	33	18.4730	.43775	7591.
11	5.9243	.14039	16673.	34	19.0434	.45126	7428.
12	6.4947	.15390	15683.	35	19.6138	.46478	7273.
13	7.0651	.16742	14820.	36	20.1842	.47830	7126.
14	7.6355	.18094	14061.	37	20.7546	.49181	6985.
15	8.2059	.19445	13388.	38	21.3250	.50533	6851.
16	8.7763	.20797	12786.	39	21.8954	.51885	6723.
17	9.3467	.22149	12244.	40	22.4658	.53236	6600.
18	9.9171	.23500	11753.	41	23.0362	.54588	6483.
19	10.4878	.24852	11307.	42	23.6066	.55940	6370.
20	11.0578	.26203	10898.	43	24.1769	.57291	6262.
21	11.6282	.27555	10522.	44	24.7473	.58643	6158.
22	12.1986	.28907	10176.	45	25.3177	.59994	6058.
23	12.7690	.30258	9855.				

Table 5. Annulus designations and nomenclature for DS1 and DS2

Data set	spectrograph	annulus subdivision	azimuth range	radial designation	radial range( $r_{L1}$ )
DS1	PRISM	center	0°-360°	—	0.000-0.075
		stream	0°-90°	0.10	0.075-0.125
		back	90°-270°	0.10	0.075-0.125
		front	270°-360°	0.10	0.075-0.125
		PRISM	stream	0°-90°	0.15
	back		90°-270°	0.15	0.125-0.175
	front		270°-360°	0.15	0.125-0.175
	PRISM	stream	0°-90°	0.20	0.175-0.225
		back	90°-270°	0.20	0.175-0.225
		front	270°-360°	0.20	0.175-0.225
	PRISM	stream	0°-90°	0.25	0.225-0.275
		back	90°-270°	0.25	0.225-0.275
		front	270°-360°	0.25	0.225-0.275
	PRISM	stream	0°-90°	0.30	0.275-0.325
		back	90°-270°	0.30	0.275-0.325
		front	270°-360°	0.30	0.275-0.325
	PRISM	stream	0°-90°	0.40	0.375-0.425
		back	90°-270°	0.40	0.375-0.425
		front	270°-360°	0.40	0.375-0.425
	PRISM	stream	0°-90°	0.50	0.475-0.525
		back	90°-270°	0.50	0.475-0.525
		front	270°-360°	0.50	0.475-0.525
	PRISM	stream	0°-90°	0.60	0.575-0.625
		back	90°-270°	0.60	0.575-0.625
front		270°-360°	0.60	0.575-0.625	
DS2			0°-360°	A	0.000-0.100
			0°-360°	B	0.100-0.200
			0°-360°	C	0.200-0.300
DS2			0°-360°	D	0.300-0.400
			90°-360°	E	0.400-0.700
			0°-90°	F	0.400-0.700

Table 6. Properties of accretion disk bright spot

parameter	value	parameter	value	parameter	value
$T_{\text{eff,rim}}$	6058K	HSAZ	20	HWDW	55
HSTEMP	14,000K	HSDWD	1	TDWND	6500K
HSUP	1	TUPD	6500K		

Note. — HSAZ is the position angle (degrees) of the center of the bright spot region, measured from the line of centers in the direction of accretion disk rotation. HWDW is the angular width of the bright spot, in degrees. HSTEMP is the temperature of the bright spot. HSDWD is the angular width (degrees) of the downwind region from the end of the bright spot to the merge point with the rim proper. TDWND is the temperature of the middle of region HSDWD. HSUP is the angular width (degrees) of the upwind region comparable to HSDWD. TUPD is the temperature of the middle of region HSUP.

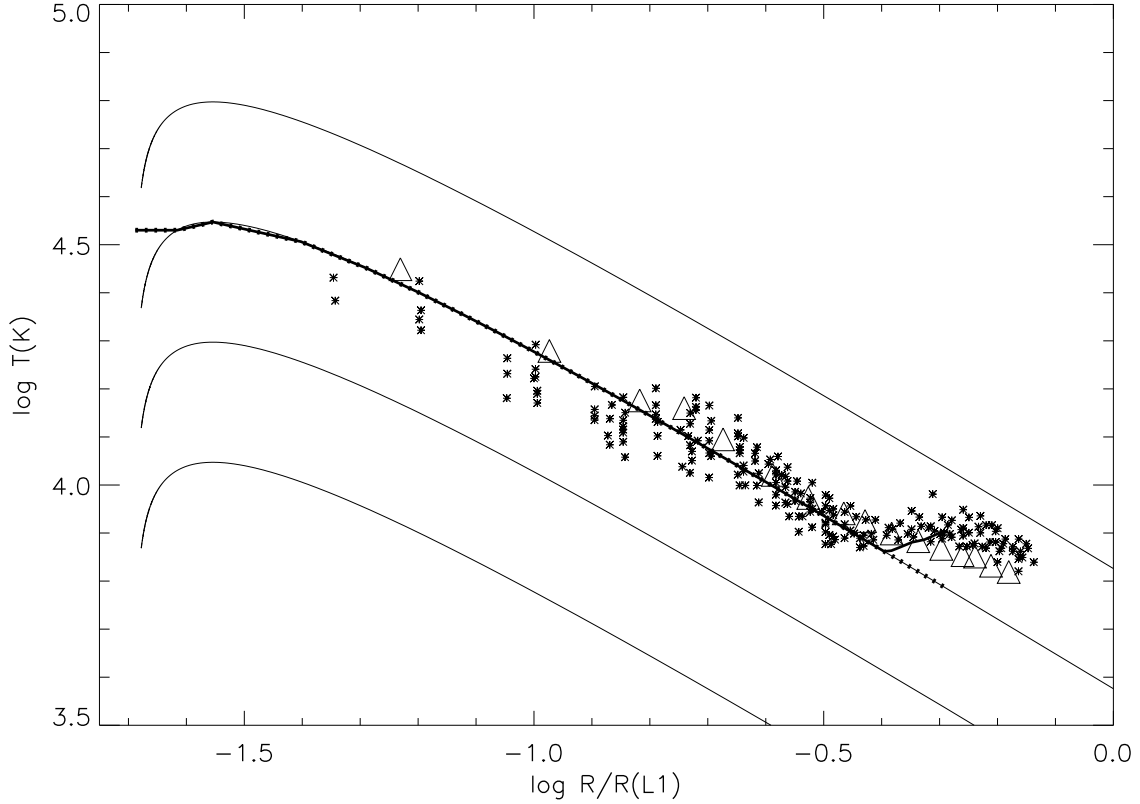


Fig. 1.— The continuous line is the  $T_{\text{eff}}$  profile for the system model, with restricted annular azimuthal sections in the outer part of the accretion disk. The dotted line is the same profile but for the remainder of the azimuthal annular sections in the outer part of the accretion disk. Crosses mark plotted points from Rutten et al. (1992, Figure 4a). Triangles mark ‘back’ side temperatures from Baptista et al. (1998) for November 1994 transformed to our adopted distance of 250pc. Continuous curves, from top to bottom, are standard models for  $\dot{M}/M_{\odot}(\text{yr}^{-1}) = 5.0 \times 10^{-8}, 5.0 \times 10^{-9}, 5.0 \times 10^{-10},$  and  $5.0 \times 10^{-11}$ . See the text for details.

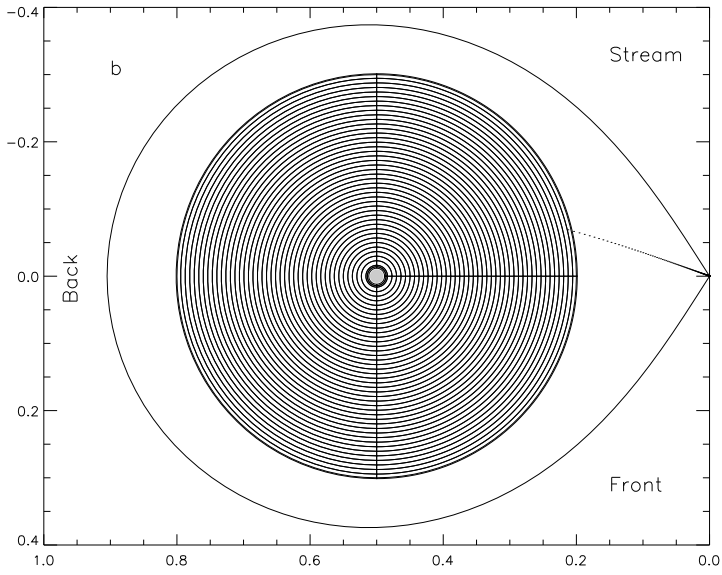
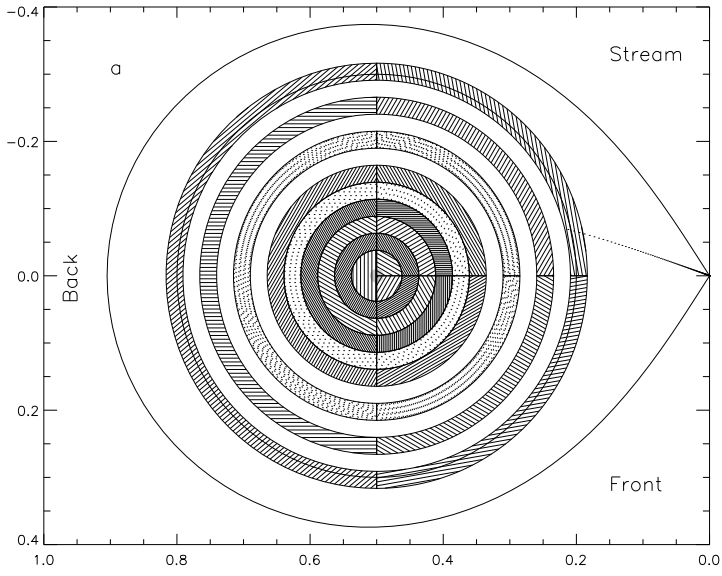


Fig. 2.— (a): Segregation of DS1 pixels into concentric rings. (b): Corresponding BINSYN model with 44 annuli.



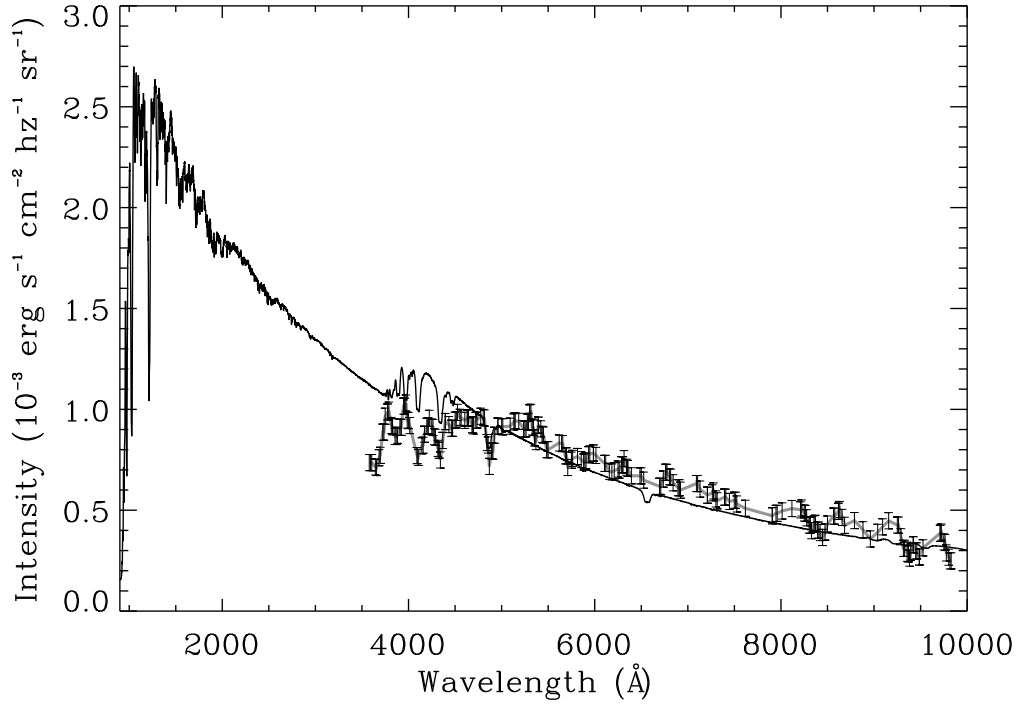
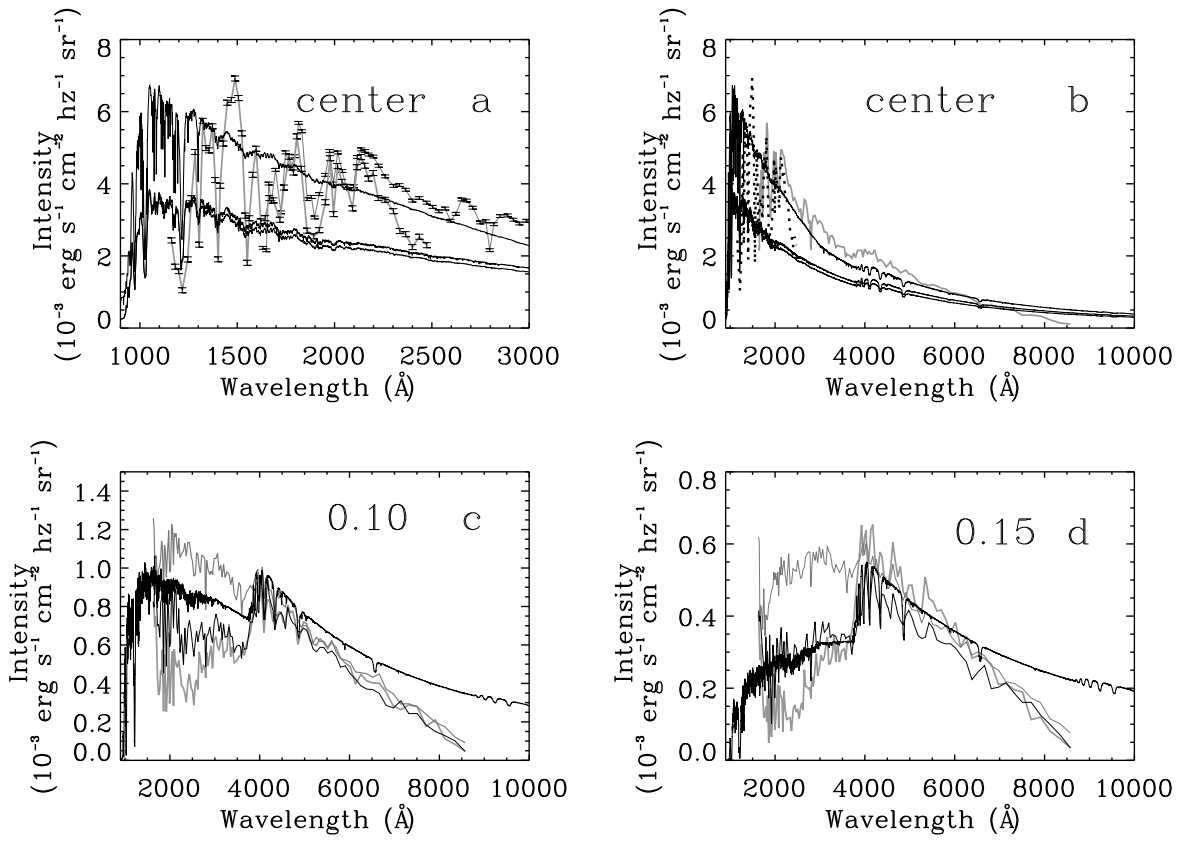
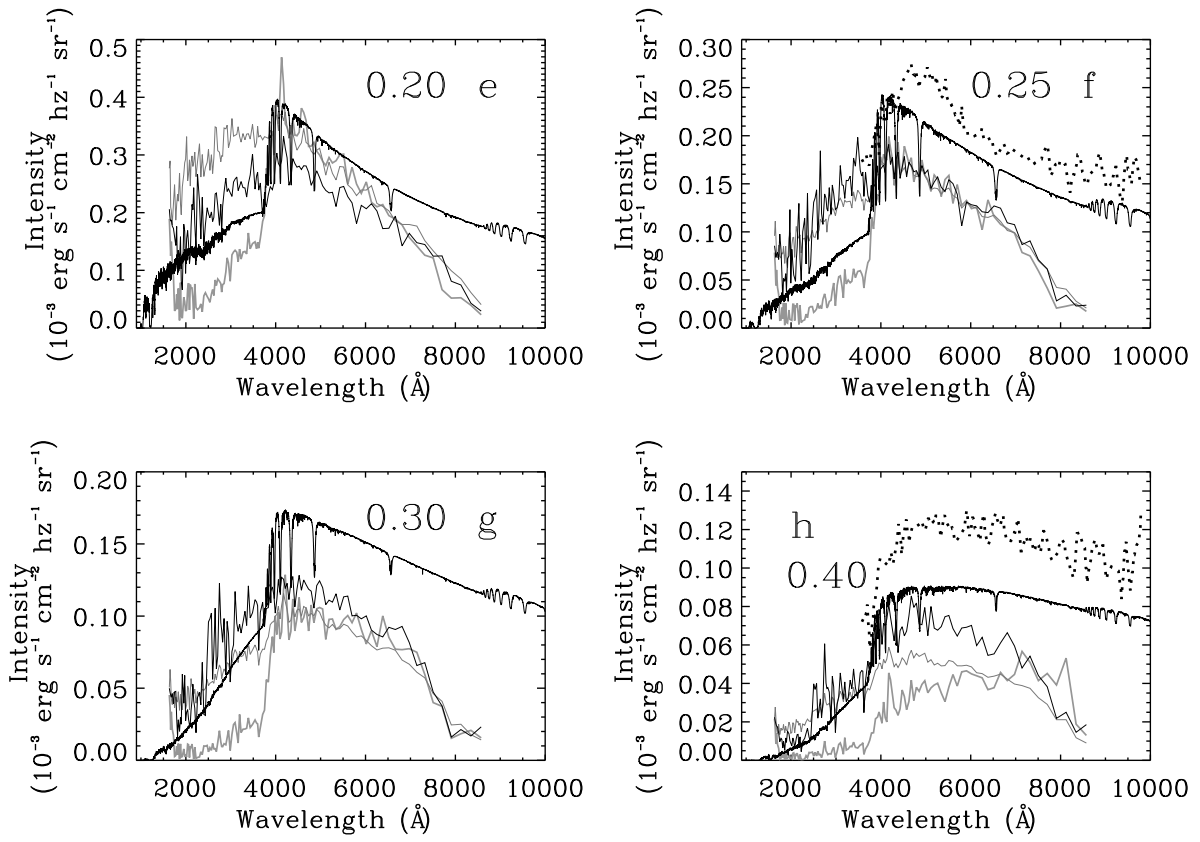


Fig. 3.— Fit to Rutten et al. (1994) central region (grey line, region A, Table 5). The continuous line is a 20,000K WD plus  $\dot{M} = 5.0 \times 10^{-9} M_{\odot} \text{yr}^{-1}$  standard model accretion disk. The accretion disk region corresponding to the observational data extends to  $0.10 r_{L1}$ , as for the model data. Except for the adopted distance used to produce the data points there are no free parameters in this fit. See the text for details.





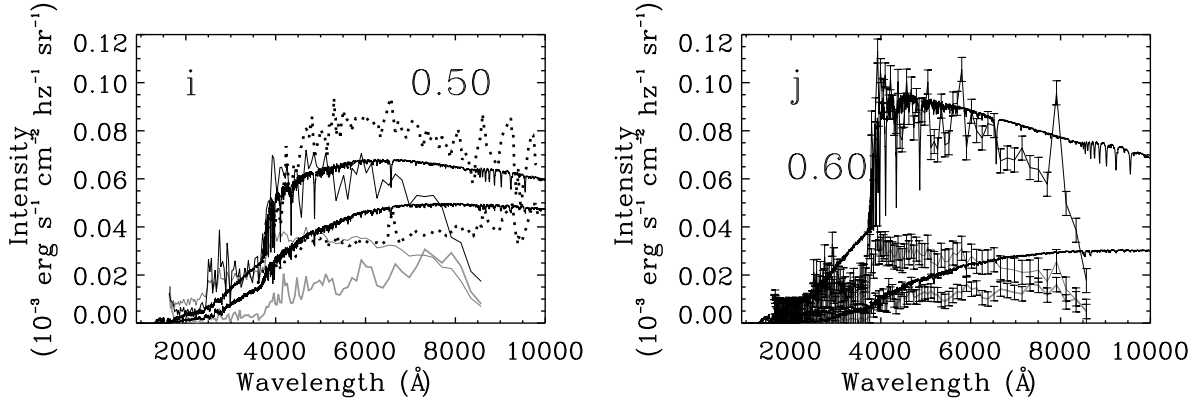


Fig. 4a-4j.— Fits of synthetic spectra to DS1 and DS2 data. In Figure 4a and Figure 4b the broad grey plot is the PRISM and the light grey plot is G160L; they are the 'center' in Table 5. In Figure 4c and thereafter the heavy grey line is the 'front', the light grey line is the 'back', and the light continuous line is the 'stream'. The heavy continuous line is the synthetic spectrum. In all cases the synthetic spectrum 'front' is the same as the 'back'. Figure 4c is radial designation (Table 5) 0.10; Figure 4d is radial designation 0.15. The dotted plot is DS2 radial designation B. Figure 4e is DS1 radial designation (Table 5) 0.20; Figure 4f is radial designation 0.25; the dotted line is DS2 radial designation C. Figure 4g is DS1 radial designation 0.30; Figure 4h is DS1 radial designation 0.40; the dotted line is DS2 radial designation D. Note that the 'stream' now is higher than either the 'front' or 'back'. Figure 4i is DS1 radial designation (Table 5) 0.50. The lower synthetic spectrum simulates the 'back' and the upper synthetic spectrum simulates the 'stream'. The lower dotted line is DS2 radial designation E and the upper dotted line is DS2 radial designation F. Figure 4j is DS1 radial designation 0.60. The lower synthetic spectrum simulates the 'back' and the upper synthetic spectrum simulates the 'stream'. Note that the DS1 'stream' greatly exceeds either the 'front' or 'back'. See the text for details.

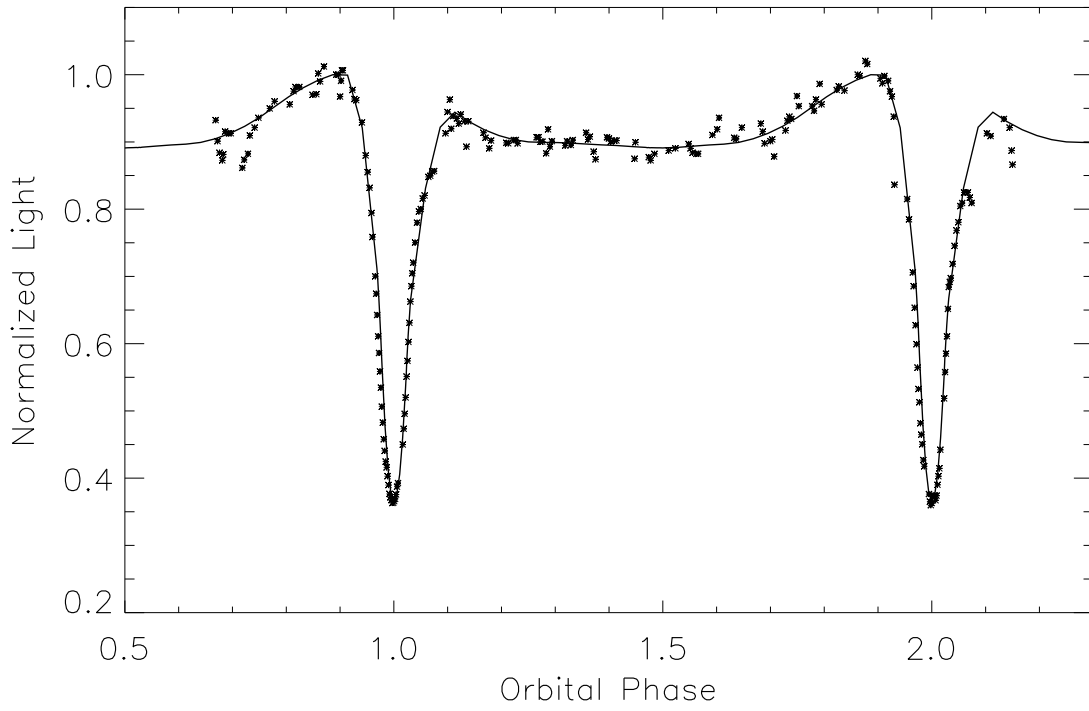


Fig. 5.— Synthetic light curve fit to V data (Walker & Herbig 1954) for May 21, 1953. See the text for details.

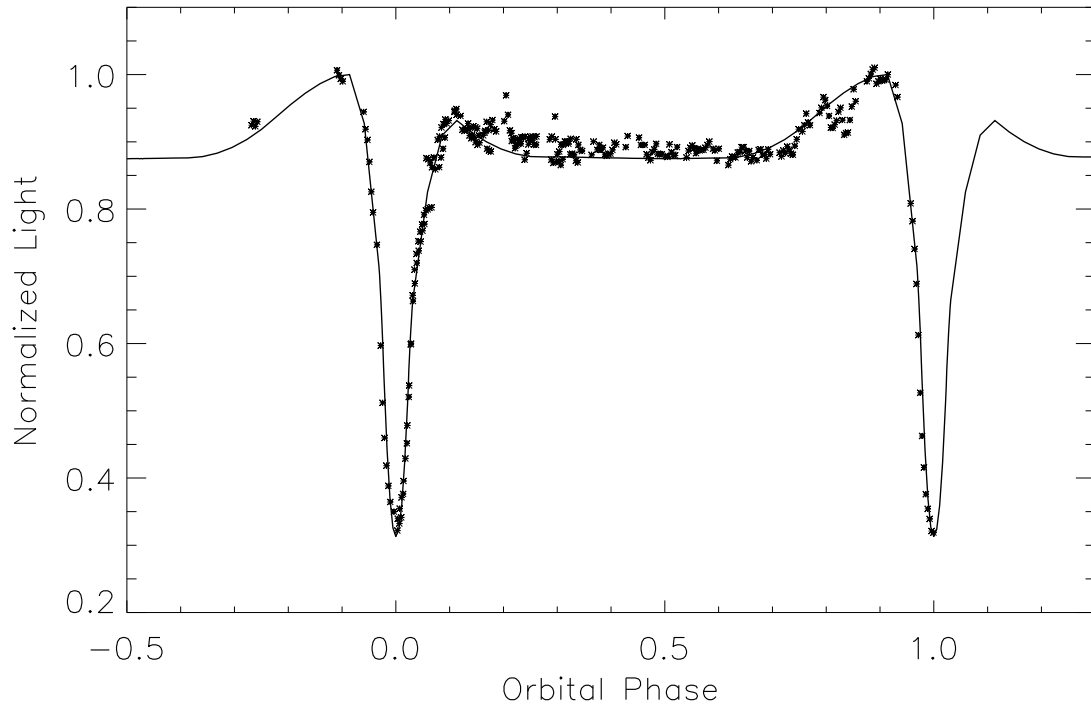


Fig. 6.— Synthetic light curve fit to B data (Walker & Herbig 1954) for April 17, 1953. Note the systematic trend in the residuals between orbital phases 0.2 and 0.8. See the text for details.

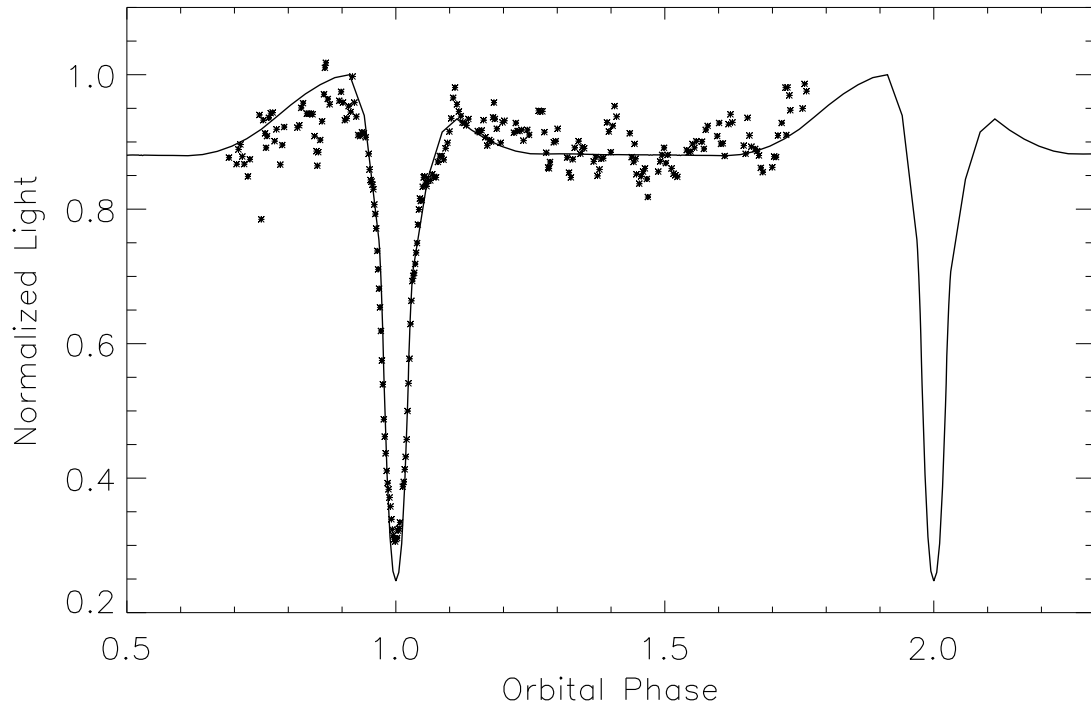


Fig. 7.— Synthetic light curve fit to U data (Walker & Herbig 1954) for June 13, 1953. See the text for details.

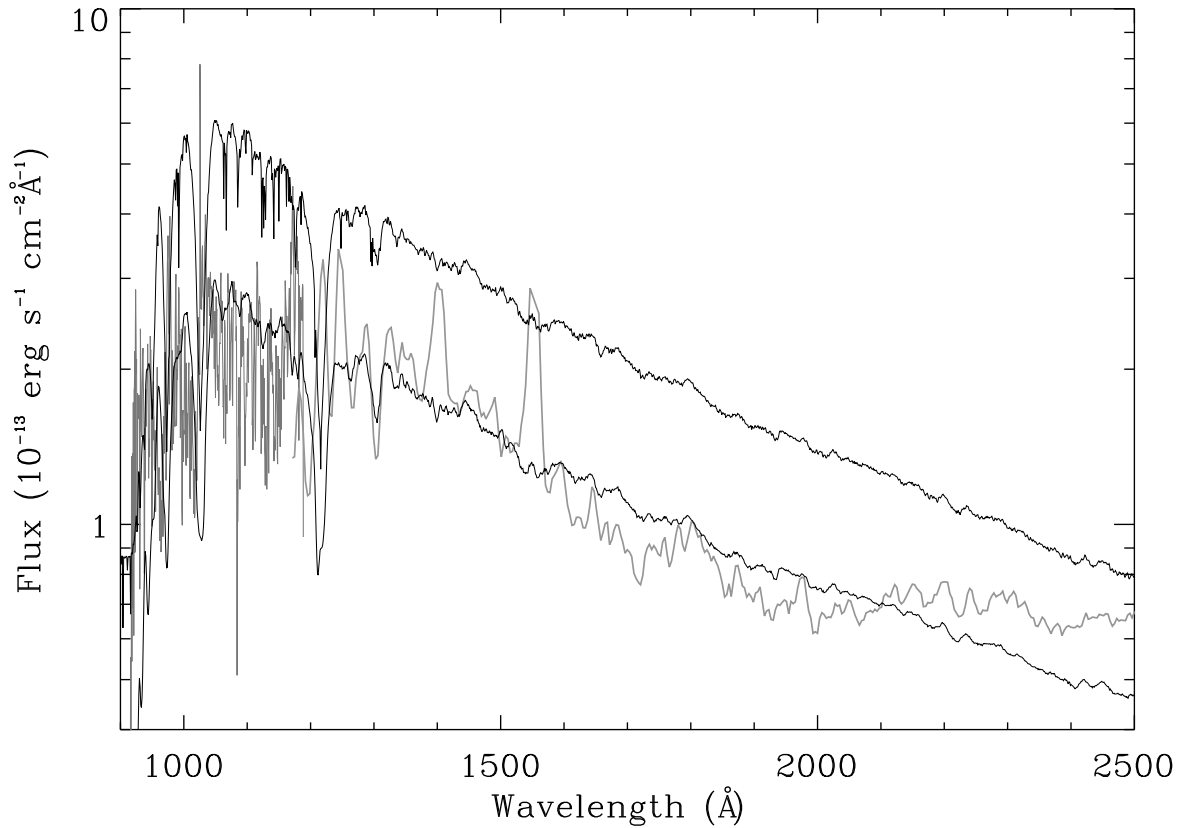


Fig. 8.— Grey line,  $\lambda > 1200\text{\AA}$ : *FOS* data set Y2AH0201T. Grey line,  $\lambda < 1200\text{\AA}$ : *FUSE* orbit04 spectrum. Upper synthetic spectrum: Model with 40,000K WD. Lower synthetic spectrum: Model with 20,000K WD. Both synthetic spectra have been divided by  $7.5 \times 10^{41}$ , corresponding to a distance of 281pc. See the text for details.



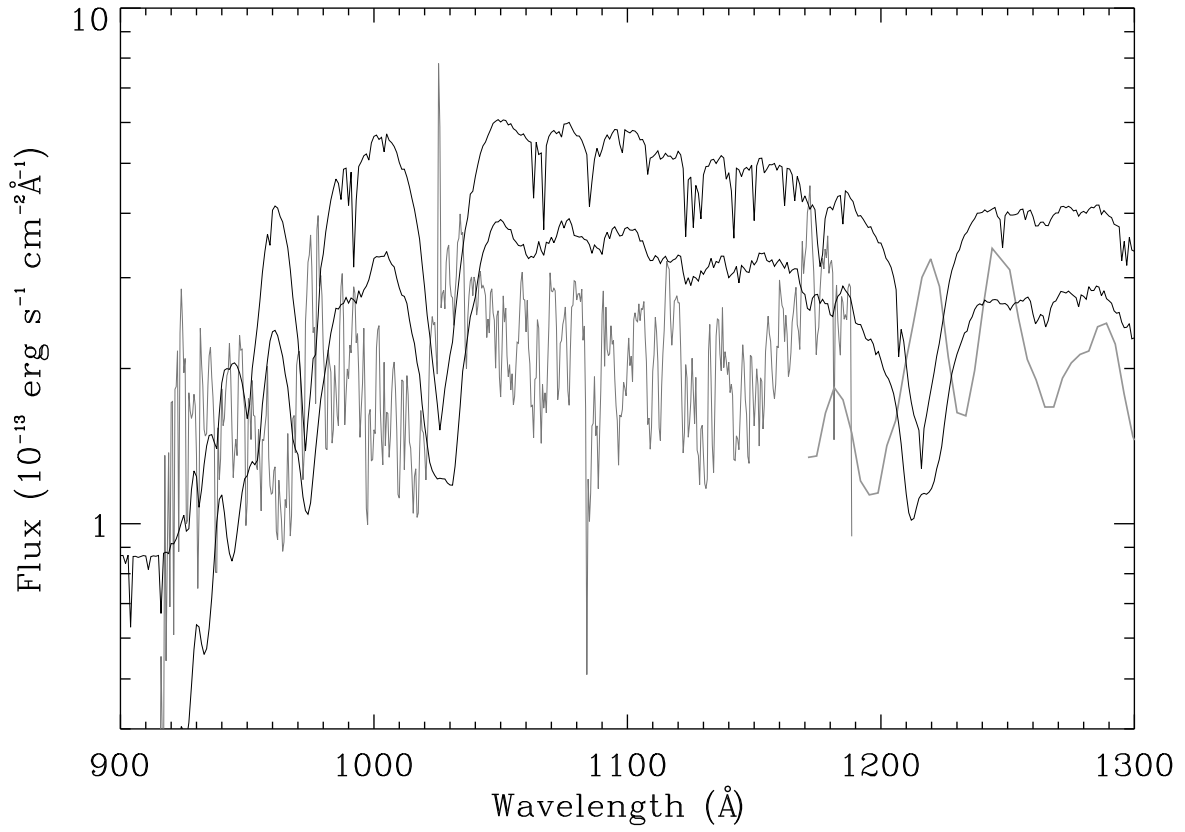


Fig. 9.— FUV plot of same data as Figure 8. Lower synthetic spectrum: Model with 20,000K WD. Upper synthetic spectrum: Model with 40,000K WD. See the text for details.

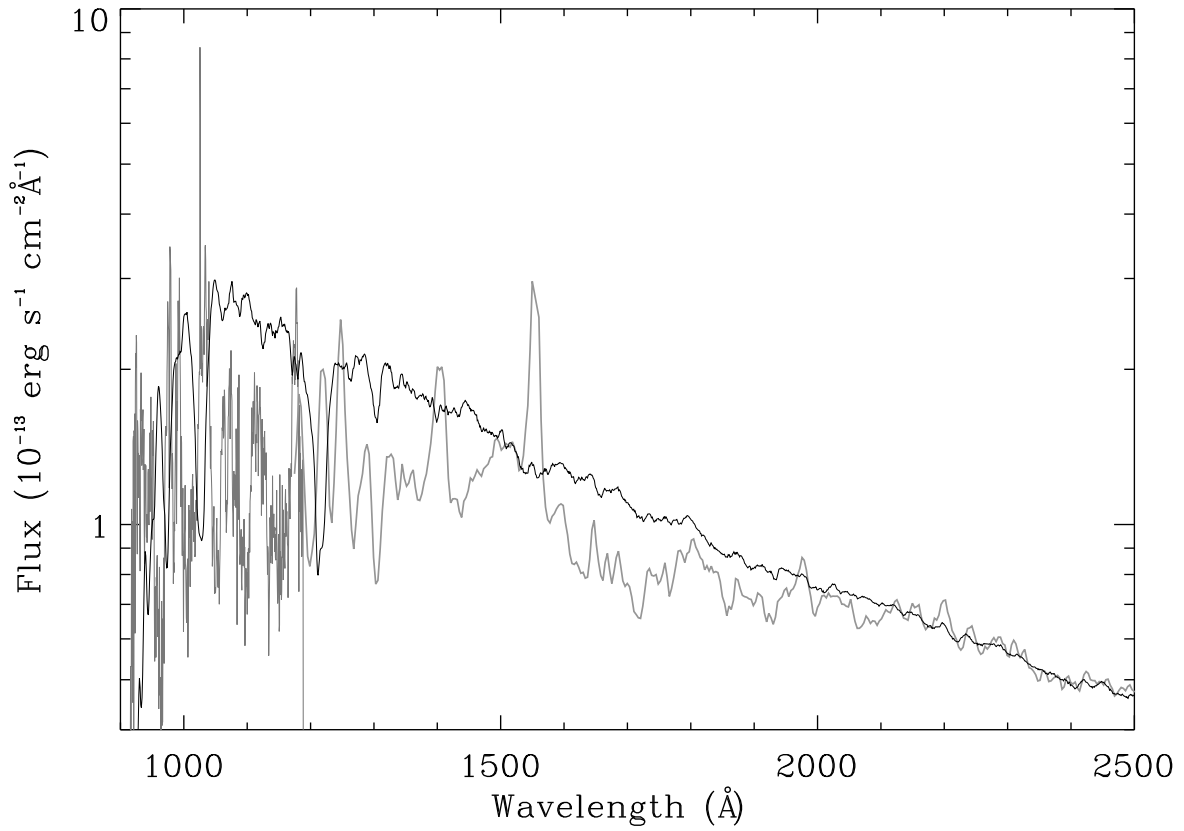


Fig. 10.— Grey line,  $\lambda > 1200\text{\AA}$ : *FOS* data set Y2AH0401T. Grey line,  $\lambda < 1200\text{\AA}$ : *FUSE* orbit03 spectrum. The synthetic spectrum, using a 20,000K WD, has been divided by  $7.5 \times 10^{41}$ . See the text for details.

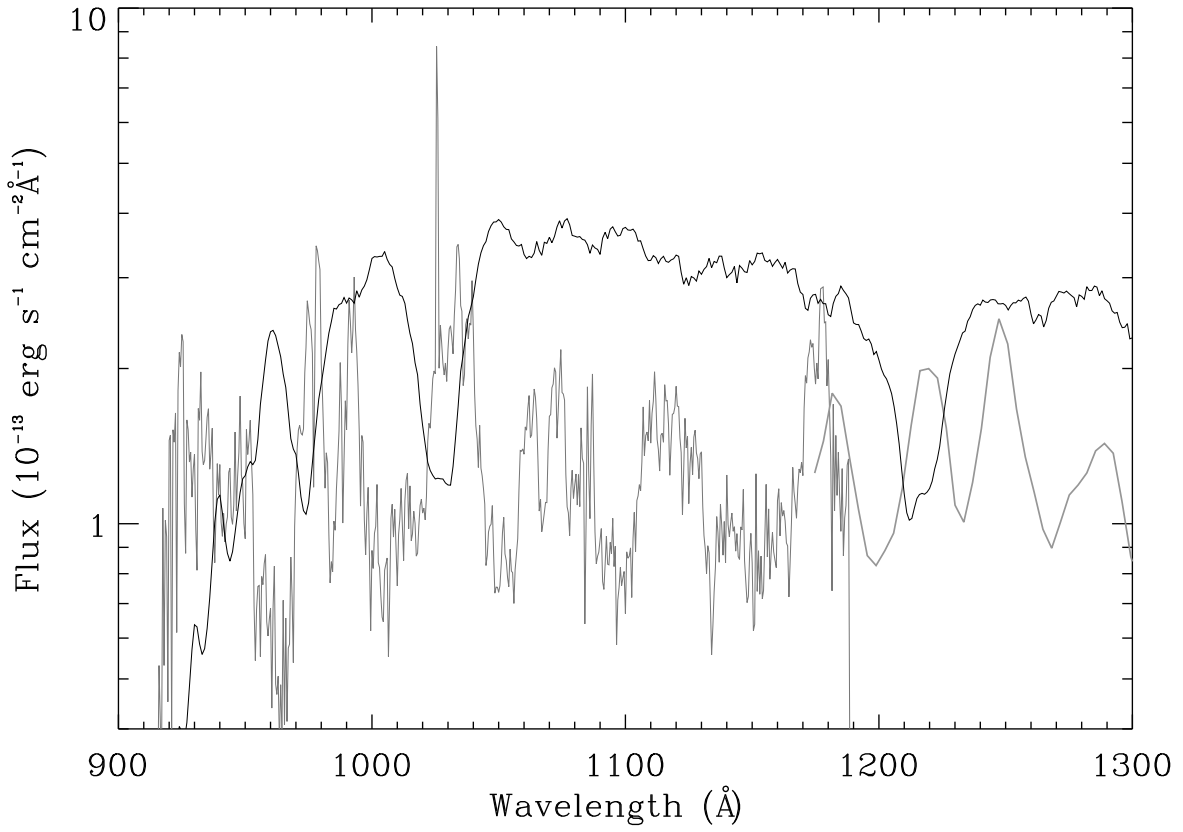


Fig. 11.— FUV detail of Figure 10. Note the contrast to Figure 9. The synthetic spectrum, using a 20,000K WD, has been divided by  $7.5 \times 10^{41}$  and plotted as the heavy line. See the text for details.

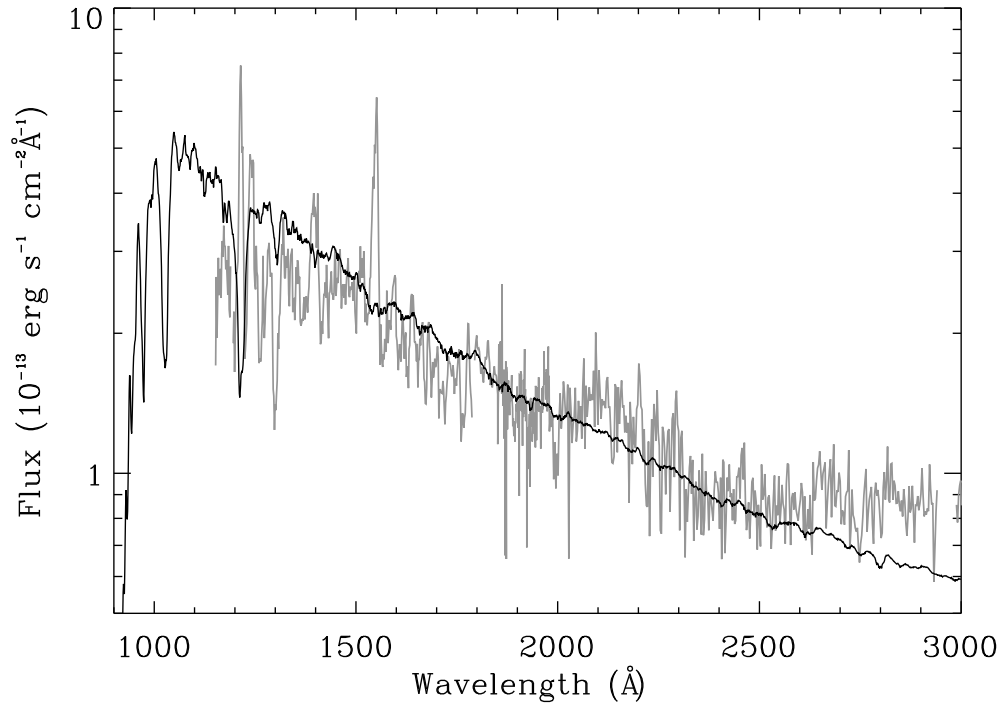


Fig. 12.— Grey line; SWP10371+LWR09051, observed 16/10/80. Heavy line: 20,000K WD and standard model accretion disk with  $\dot{M} = 5.0 \times 10^{-9} M_{\odot} \text{yr}^{-1}$  mass transfer rate and at a distance of 234pc. See the text for details.

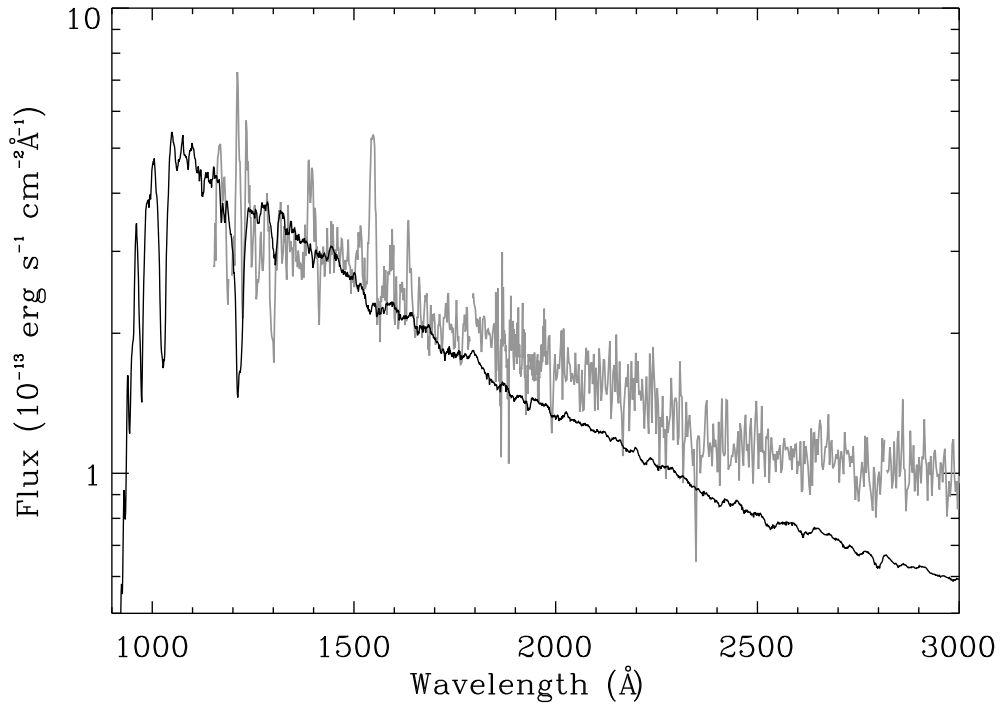


Fig. 13.— Grey line: SWP10128+LWR08799, observed 14/09/80. Heavy line: 20,000K WD and standard model accretion disk with  $\dot{M} = 5.0 \times 10^{-9} M_{\odot} \text{yr}^{-1}$  mass transfer rate and at a distance of 234pc. See the text for details.

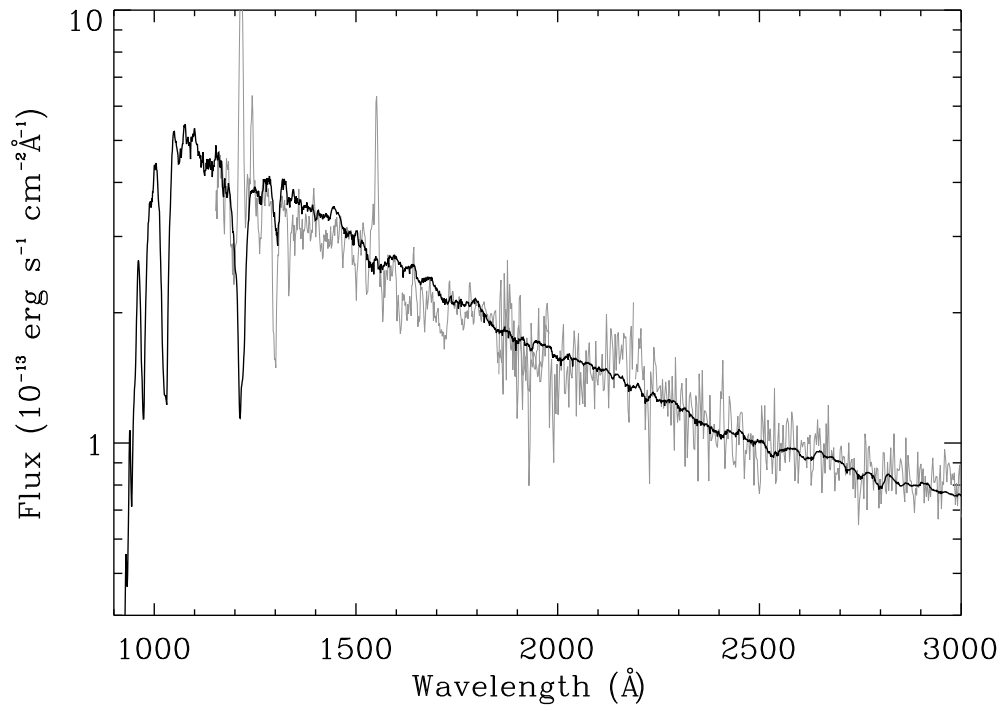


Fig. 14.— Grey line: SWP10677+LWR09388, observed 25/11/80. Synthetic spectrum: 20,000K WD and standard model accretion disk with  $\dot{M} = 3.0 \times 10^{-9} M_{\odot} \text{yr}^{-1}$  mass transfer rate and at a distance of 165pc. See the text for details.

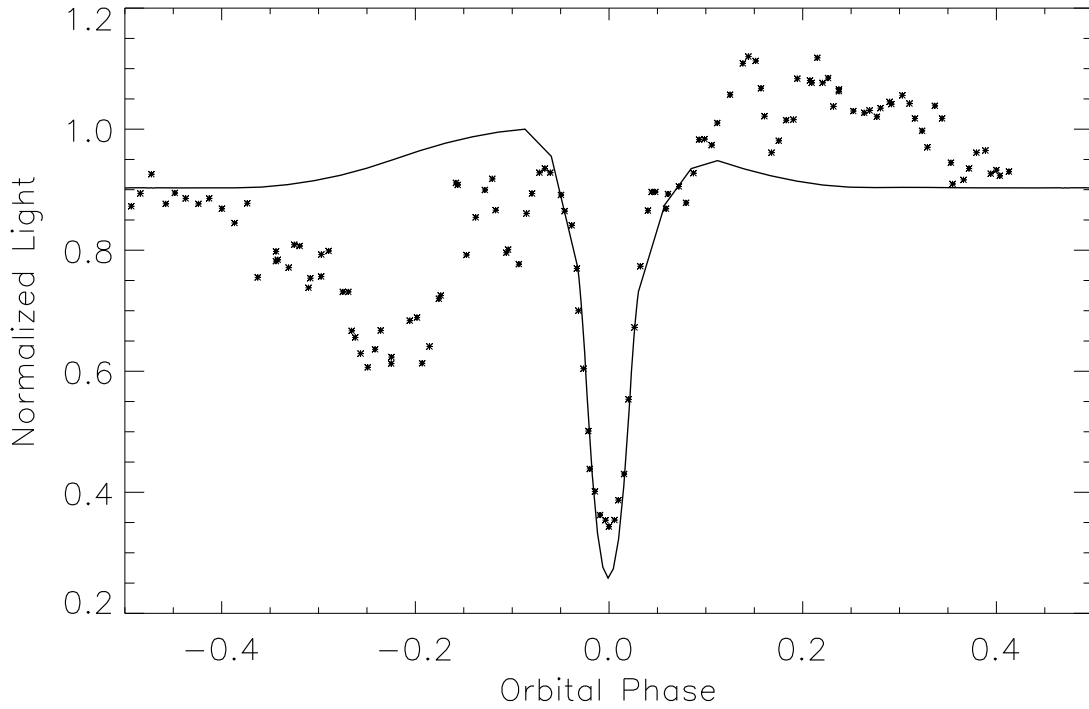


Fig. 15.— Fit of synthetic light curve of Figure 7 to an observed U light curve for May 29, 1952 (Johnson, Perkins, & Hiltner 1954). An extreme discrepancy from the system model, with light maximum occurring *after* eclipse. See the text for a proposed explanation.